Society For Biomaterials

CLEMSON BIOENGINEERING

BioMEDS
Biomedical Engineering Development Society

CBS
CLEMSON BIOENGINEERING SOCIETY

Bio Materials Day

Clemson University - October 1, 2011 - Madren Center - Clemson, SC

Abstract Booklet

Society For Biomaterials

CLEMSON
BIOENGINEERING

BioMEDS
Biomedical Engineering Development Society

CBS
CLEMSON BIOENGINEERING SOCIETY

BioMaterials Day

Clemson University - October 1, 2011 - Madren Center - Clemson, SC

Poster Presentation Abstracts

Optimizing the Direct Syntheses of Polyethylenimine-capped Metallic Nanoparticles - Abstract

Scott Cole, Fiaz Mohammed, and Dr. Christopher Kitchens

Clemson University Department of Chemical and Biomolecular Engineering

The biocompatible properties of metallic nanoparticles have been studied recently for their possible applications in imaging, diagnostics, cancer treatment, and numerous other fields.[1] Polyethenimine (PEI) can act as a surfactant on the particles in order to stabilize the syntheses. Both gold and silver nanoparticles were tested, and procedures for the synthesis of cationic, stable particles were ultimately deduced. The gold nanoparticles were prepared in a simple manner, dissolving a designated amount of metal in deionized water, and adding the PEI ligand after the metal reduction via sodium borohydride. Conversely, silver nanoparticles functionalized with PEI were prepared adding the ligand to the metal before the reduction phase. After sufficient stirring, both metals' syntheses were centrifuged in order to crash out the particles and redisperse them in a more pure solvent, with minimal excess ligand. The pH of the final solvent proved to be a critical variable to manipulate in order to minimize aggregation, enhance optical properties, and optimize stability. All prepared syntheses were characterized with UV-Vis spectrometry, along with follow up analysis with dynamic light scattering (DLS), zeta potential, and transmission electron microscopy (TEM). The optimal PEI-capped gold nanoparticle synthesis had a ligand concentration of .05wt% (~.8mM; PEI~600g/mol) and a .25mM metal concentration. The syntheses for the positively-charged gold and silver nanoparticles will be utilized; primarily, their potential effects on different proteins will be studied. Ultimately, the unique way that this chain of amines functionalizes a nanoparticle as a stabilizing agent could be used in the biomedical field to aid in the treatment of disorders or possibly the enhancement of the workings of human biology.

References

1.   E. Boisselier and D. Astruc, *Chem. Soc. Rev.*, 2009, **38**, 1759–1782.

Design of an Anatomical Cervical Orthosis Testing Apparatus and Preliminary Results

R. Maglin Halsey[1], Kaitlyn M. Harfmann[1], Emanuel Nuwass[2], Dilantha B. Ellegala[3], Joyce S. Nicholas[3], Delphine Dean[1], John D. DesJardins[1]

[1]Department of Bioengineering, Clemson University 29634
[2]Haydom Hospital, Tanzania, Africa, [3]Medical University of South Carolina 29425

Cervical collars are prescribed for suspicion of injury, stabilization, and relief of pain. With supplies of these devices limited or nonexistent in the developing world, our clinical partners in Tanzania have developed a woven grass alternative that is hoped to provide a clinical benefit. The goal of this project was to design an anatomically accurate cervical orthosis mechanical testing platform, and then evaluate orthosis designs.

Our test platform consists of a fiberglass mannequin head and metal-reinforced fiberglass thorax that are connected via a flexible neck composed of four universal joints attached in series surrounded by foam. A loading affecter made of aluminum rods passes through the head, and connects directly to the "cervical" universal joints that then connect to a transverse aluminum rod in the thorax. Resulting ranges of motion allow the analysis of collar stiffness in flexion/extension ($\pm140°$), lateral flexion ($\pm90°$), and axial rotation ($\pm30°$).

Cervical collars were placed on the mannequin, and neck length was adjusted to achieve a clinically relevant fit. Weights were used to produce physiologic moments (0-5Nm) about the neck. Initial tests of a clinical "stabilization" collar design (Ossur Philadelphia Tracheotomy) yielded torsional stiffness measures of 0.044Nm/° (1.45Nm@33° extension), 0.033Nm/° (1.45Nm @ 43° lateral flexion), and 0.16Nm/° (1.14Nm@7° axial rotation). Initial woven grass collar designs did not provide effective restraint and design improvements are being recommended to our Tanzanian clinical partners for improved patient treatment.
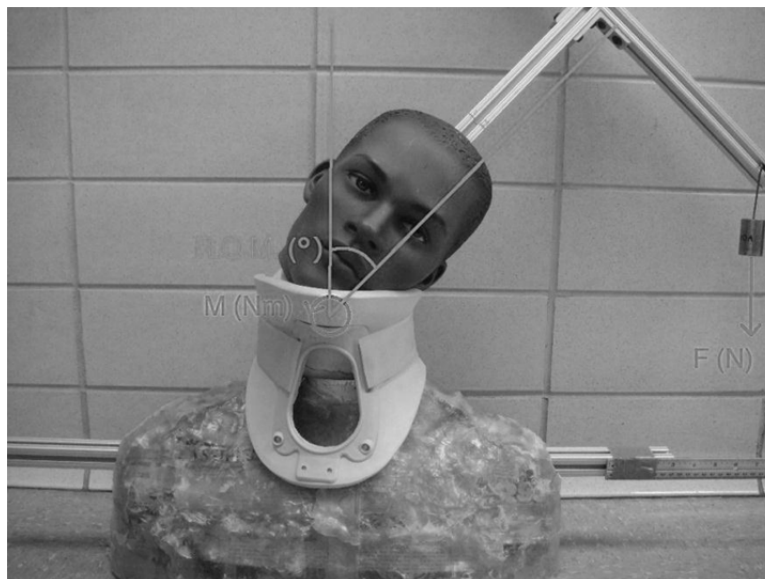

Figure 1. Anatomical Cervical Orthosis Testing Apparatus

Magnetic Cell Spheroid for Tissue Engineering Applications

Laura Reese, Brandon Mattix, Trey Poole, Rick Visconti, Dan Simionescu, Agneta Simionescu, Linda Jenkins, Terri Bruce, Frank Alexis.

Bioengineering Department, Clemson University, Clemson, SC 29631

The objective of the proposed research is to integrate magnetic properties into the fabrication of cell spheroids, utilizing magnetic forces for self-assembly. Initial studies have been performed to show that we can 1) Fabricate magnetic cell spheroids 2) Avoid toxic effects of iron oxide nanoparticles on cells for a long period of time, and 3) Control the IO location within the spheroid 4) Magnetically manipulate spheroids. Future studies will look at the fabrication of linear and branched blood vessels while using magnetic forces to promote maturation and control the cell phenotype.

Undergraduate Student Abstracts

Assessment of Horse-Rider Kinematic Variables During Hippotherapy

Meredith Cole [1], Justin Arnosky [1], Beryl Walker[2], Simone Neuhoff [3], Rick Blob [4],
Kristine Vernon [2], John D. DesJardins [1]

[1] Department of Bioengineering, [2] Department of Animal and Veterinary Sciences,
[3] Department of Mechanical Engineering, [4] Department of Biological Sciences
Clemson University, Clemson, SC

Statement of Purpose:
Hippotherapy is a novel rehabilitation therapy that utilizes a horse as a moving platform for the treatment of physical or neurological conditions. The patient is placed on the horse's back and performs a variety of activities including stretching exercises, range of motion tests, and games while the horse is led around an arena. The motion that the horse provides is a crucial part of the treatment, yet the biomechanical interaction between horse and rider in a hippotherapy situation is largely unknown.

Previous studies have found that conformational aspects effect the movement of the equine back. It is also accepted that horses display differing motions in their back depending on their conformation and movement. Horses can be evaluated by eye for their movement kind and classified accordingly. The parameters commonly used for this are the hindlimb activity, hock action, freedom of the shoulder and length of stride. Significant differences have been found in the movement of horses visually judged to be "good" and "poor" quality. The rider is directly influenced by the motion in the horses back. This motion is dependent on the horse's conformation and movement type, which can be identified by a trained eye. The purpose of this experiment was to evaluate the relationship between horse and rider kinematics during hippotherapy.

Methods:

A Biometrics motion system (SG150, Cwmfelinfach, Gwent, United Kingdom) was used to measure the angle in the thoracic and lumbar spine and both hips while the horse was lead on a straight path at the walk. A video capture motion analysis system was used to capture the horse's motion. The combined instrumentation is shown in figure 1.

Figure 1: Instrumentation of horse and rider

Results:

The horse produces cyclical motion in monitored joints corresponding to the stride phase. For one subject the mean range of motion in the thoracic vertebra over 11 strides is 3.16 degrees with a mean minimum and maximums of 4.5 and 1.3 degrees to the left respectively with a standard deviation of 1.14 and 1.45 as shown in Table 1.

Table 1: Summary of Thoracic Bending

	Thoracic Lateral Bending, Right +												
	Trial 1/Pass 3						Trial 4/Pass 3					Mean	St Dev
Stride	1	2	3	4	5	6	1	2	3	4	5		
Minimum	-3.8	-2.9	-3.4	-4.1	-3.8	-3.2	-5.8	-6	-5.5	-5.3	-5.5	-4.48	1.15
Maximum	0.7	0.2	0.3	-0.4	-0.6	-1.2	-2.8	-3.2	-3.2	-2.4	-1.9	-1.32	1.45
Range	4.5	3.1	3.7	3.7	3.2	2	3	2.8	2.3	2.9	3.6	3.16	0.70
Cadence (sec)	1.23	1.23	1.225	1.23	1.225	1.225	1.23	1.23	1.225	1.23	1.23	1.23	0.00

Discussion:

This study found that repeatable motion analysis data collection was possible for both horse and rider with this methodology. The 2D video capture method combined with the human biometrics system provided a large dataset from which to begin extracting correlations in kinematic variables between the horse and rider motions.

Friction Testing of Stainless Steel Micropatterned Surfaces for Orthopaedic Bearing Surfaces

C. J. Eljach[1], N. Mitchell[2], B. Lodge[2], J. Sharp[3], M. Kennedy[2], and J. D. DesJardins[1]
[1]Department of Bioengineering, [2]School of Materials Science and Engineering,
[3]Department of Mathematical Sciences, Clemson University, Clemson, SC

Statement of Purpose:
Friction and wear are the result of physical interactions between two materials as they contact and slide against each other. Characteristics such as the materials' surfaces, geometrical shapes, contact load, and environment will affect how the materials interact. Biomaterials used for total joint replacements undergo friction and wear during movements such as walking. Limited biocompatibility of suitably wear resistant total joint replacement materials has fueled the innovation of novel surface treatments for enhanced tribological outcomes in existing biomaterials. This study investigates the use of stainless steel surface micropatterning for total joint replacement; we hypothesize that surface micropatterning of the metal can positively influence contact friction and damage surface to enhance the durability of the bearing surfaces for in vivo use.

Methods:
For this study, 316L stainless steel plates were subjected to a proprietary micropatterning processes (Hoowaki LLC, Pendleton, SC) that resulted in eight different micropatterned surfaces of either depressions (circular and oval) or pillars (circular, oval, and square). A chrome steel ball bearing and flat surfaced polyethylene pin (UHMWPE GUR 1020) were used as counterface bearing surfaces. Surface roughness was measured before and after each tribological test using a non-contact white light surface interferometer ((WYKO NT-2000, Veeco, Inc. Tucson, AZ). The tribological tests were performed using a CETR UMT-2 (Campbell, CA). Surface micro-features were assessed for height, depth and width, and contact surface area was calculated as the ratio of the area in contact with the ball on the micropatterned surface as compared to that of a non-patterned surface. Ball on flat and flat on flat set ups were performed using a 20N bi-axial load cell to measure the coefficient of friction between metal on metal and metal on polymer friction for both single pass and reciprocating sliding. Tests were performed at room temperature with a normal load of 15N, a pin velocity of 10mm/sec with a 2cm path length and a 50-cycle reciprocal sliding assessment of friction. Samples were tested under dry and lubricated conditions using Cannon Instrument Company oil standards (batch N35, State College, PA) as the lubricant.

Results:
Surface feature analysis showed that the manufacturing process produced distinct surface feature heights, depths and widths for each pattern. During sliding, the coefficient of friction varied for each feature, but the results for the ball bearing and polyethylene tests were similar. As the micro-patterned depression hole size increased in width, the coefficient of friction decreased for both dry and lubricated runs. The pillared surfaces showed the opposite effect in that as the pillar features increased in width, the coefficient of friction increased (as seen in Figure 1). As seen in the results, there is a trend showing that the micropatterned surfaces featured on the stainless steel can have a positive effect on the surface coefficients of friction.
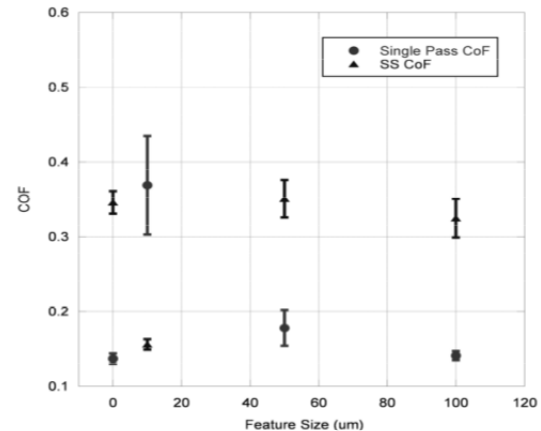

Figure 1: The round depression diameter influences the initial Coefficient of friction, but more importantly it shows that this initial Coefficient of friction is not an indicator of the SS Coefficient of friction for the ball bearings. The non-patterned samples are shown as zero feature size.

Conclusions: Stainless steel balls and flat polyethylene pins articulating against 316L stainless steel plates with different micropatterns formed onto their surfaces were investigated in this study. The frictional behavior was found to strongly depend upon the size and shape of the micropatterned surfaces. It was concluded that single-pass metal ball articulation over circular surface micro-patterned geometries yielded lower coefficients of friction with larger depression sizes and larger pillar sizes. However, for reciprocating pass testing it lowered the coefficient of friction with smaller depression sizes and larger pillar sizes. Single-pass polyethylene pin articulation over circular geometries yielded lower coefficients of friction with larger depression sizes, yet for reciprocation pass testing it lowered the coefficient of friction with smaller depression sizes and larger pillar sizes. These positive results encourage further research to be completed on the use of micropatterning for artificial joint articulating materials.

Wear Particle Analysis: Highly Crosslinked Vitamin E Blended UHMWPE and Direct Compression Molded UHMWPE *from in-vitro ISO-14243-1 wear simulation of the DJO 3DKnee System*

John C. Ivester, Jonathan B. Matheny, Cameron E. Golightly, John D. DesJardins.
Clemson University Department of Bioengineering

Statement of Purpose: When Vitamin E is added to Ultra-High Molecular Weight Polyethylene (UHMWPE) during the manufacturing process, its antioxidant properties work to inhibit molecular chain oxidation that has been shown to influence the wear rate of this material [1]. Aged vitamin E doped highly cross-linked (HXL+VitE) UHMWPE has been shown to reduce wear for pin on disk testing, hip implants, and knee implants [2-4]. In a previous study, Vaidya *et al* conducted at 5 million cycle wear test using a load-controlled ISO-14243-1 knee simulator comparing highly cross-linked (HXL) Vitamin E (VitE) blended UHMWPE to Direct Compression Molded (DCM) UHMWPE(3DKnee system, DJO Surgical, Austin, TX). HXL+VitE UHMWPE was shown to have a significantly lower gravimetric wear rate than DCM UHMWPE (1.9 ± 1.9 mg/million cycles vs. 4.4±3.0 mg/million cycles, respectively, p<0.01) [1]. UHMWPE wear particle analysis can enhance the experimental findings of in vitro wear tests, in that the particles' characteristics (number, size, and shape) are known to affect the foreign body response [5-6] and can therefore add clinical insight into the effect of these wear rates on implant in vivo longevity. Characterization of the particles' specific geometrical features was conducted to provide a more thorough particle morphology assessment. To our knowledge, this is the first study to analyze the wear particles of aged highly cross-linked UHMWPE blended with vitamin E from TKR inserts after knee simulation.

Methods: Wear simulation was performed on aged HXL Vitamin E blended UHMWPE and DCM UHMWPE with 25% Fetal Calf Bovine Serum and 0.2% Sodium Azide as lubricant. Following 2.5 million cycles of testing, lubricant from the previous half million cycles was removed from the simulator. Wear particles within the lubricant solution were then isolated with the aid of HCl through a filtration process according to Niedzwiecki et al [7]. Following filtration, particles were imaged with a SEM at 60 various points per material. Image analysis was then performed to analyze size descriptors (equivalent circular diameter (ECD), area, and perimeter) and shape descriptors (aspect ratio, roundness, and form factor) for both types of UHMWPE and compared. Particle number was calculated using the particles' ECD and the gravimetric wear rates from Vaidya, *et al.*

Results: The number of wear particles for HXL+VitE UHMWPE was found to be 5.03 X 10^{10} particles per million cycles and 9.33 X 10^{10} particles per million cycles for DCM UHMWPE. The majority of both HXL+VitE and DCM particles had an AR less than 2.39 (74.6% for HXL+VitE, 74.4% for DCM). Size and shape descriptor values for DCM and HXL+VitE UHMWPE had very similar magnitude and distributions.
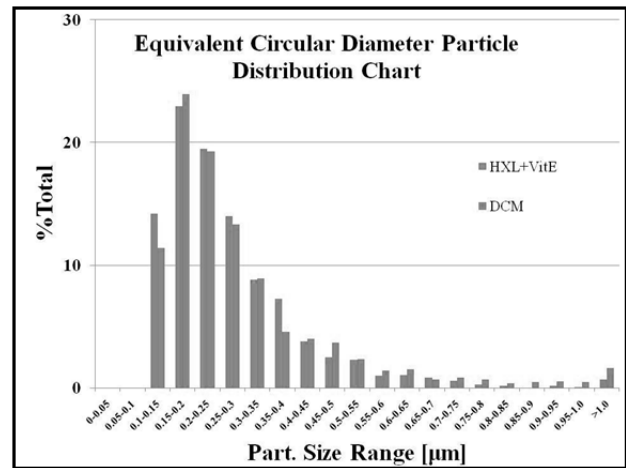

Figure 1. Percent total across ECD size ranges for DCM and HXL+VitE UHMWPE wear particles

Conclusions: From the results of this study it has been shown that HXL+VitE UHMWPE has a much lower concentration of wear particles compared to DCM UHMWPE wear particles. It has also been shown that HXL+VitE UHMWPE wear particles were similar to DCM UHMWPE wear particles in terms of size and shape. The comparison of the size descriptors (ECD, area, and perimeter) between DCM and HXL+VitE using ANOVA were statistically different due to the sheer number of particles analyzed. The values for the size descriptors for DCM and HXL+VitE have similar magnitudes for mean, median and range. In terms of pathology, the DCM UHMWPE tibial insert could be hypothesized to cause a greater pathologic response than the HXL+VitE insert due to a high particle concentration [6]. Both sets of UHMWPE particles were within the 0.1-10 μm particle diameter size range. Wear particles in this size range have been shown to cause osteolysis leading to aseptic loosening of the implant due to macrophage ingestion but will not initiate foreign body giant cell responses [5]. Both aspect ratio and roundness for DCM and HXL+VitE were not statistically different while form factor was statistically different. The DCM and HXL+VitE values for all three shape descriptors were again very similar in magnitudes for mean, median and range. A particle aspect ratio above 2.39 is considered more likely to cause a pathologic response [8]. The majority of both types of materials examined fell well below this value.

References: [1] Vaidya C, *et al. JEIM*, 2011. [2] Oral E, *et al. J. Arthroplasty*, 2006. [3] Oral E, *et al. Biomaterials.* 2004. [4] Teramura S, *et al. J. Orthop. Res.*, 2008. [5] Steinback MJ, *et al. UHMWPE Biomaterials Handbook 2nd ed*, 2009. [6] Utzschneider S, *et al. Acta Biomater.,* 2009. [7] Niedzwiecki, *et al. J. Biomed. Mater. Res.,* 2001 [8] Punt, *et al. Acta Biomater.,* 2011

The Effect of Mineral Microparticles on Dental Cell Differentiation

Amanda Farley, Laura Datko, Dr. Delphine Dean
Clemson University Department of Bioengineering

Introduction: With the progression of regenerative medicine, bio-fillers are becoming a very viable option in the treatment of dental caries and the repair of cranio-facial injuries. Much research in literature has been done on the possibility of using apatite minerals in bio-fillers to stimulate positive growth and differentiation in bone cells. Most of the previous studies have focused on bone marrow stem cells (BMSCs) cultured with micro-Hydroxyapatite (HA) particles. However, there have been mixed reports on these particles having positive or negative effects on cell differentiation to BMSC. This work delves into the effects of micro-HA on BMSCs, 7F2 osteoblasts, and dental pulp stem cells (DPSCs) as well as the effects of micro-Fluorapatite (FA) on these cells.

Materials and Methods: Alkaline phosphatase (ALP) and bicinchoninic acid (BCA) assays were run for days 1, 3, 5, 7, and 14 on the three types of cells cultured in mineral particles in order to determine the protein content. Cells were cultured 2500 cells/well with 10 ul of 10 mg/ml mineral particle in 16-well plates. Antibody stains were carried out to determine osteocalcin and collagen I production over a two week period. Rabbit anti-osteocalcin and rabbit anti-collagen I were used as primary antibodies while 488 goat anti-rabbit was used as a secondary. In addition, confocal imaging was done using collagen I and osteocalcin. Separate cultures were stained with alizarin red to ascertain the presence of early calcification within two weeks. Finally, lysates were collected from cell samples and western blots were run using protein content data gathered from BCA assays.

Results and Discussion: The ALP and BCA assays yielded mixed results. Different kinds of cells reacted differently to the added mineral; most notably the DPSCs, which had almost five times the amount of ALP specific activity on day seven than did the BMSCs or osteoblasts. Generally, the control cells had higher levels of activity than those cultured with particles with the exception of osteoblasts with HA and FA, both of which had higher activity levels throughout the 14 day period. There was a spike in collagen and osteocalcin production on day 5, and a marked increase of collagen on day 5 for osteoblasts cultured with FA. The microscope images taken from micro particle cells also yielded interesting observations. Over time the cells tended to congregate closer to the HA particles in the center of the well, while FA cells moved towards the sides of the wells where small groups of them clustered around "straggler" FA particles (Fig. 1). DPSCs and osteoblasts cultured in HA grew more rapidly and were confluent by day 7 compared to those cultured in FA.
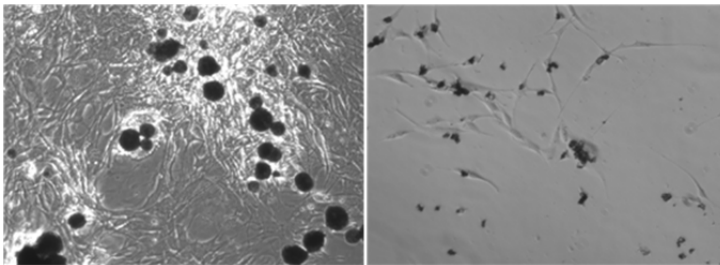

Figure 1: A dense cell population is congregated around HA particles (on the left). Conversely FA cells were more spread out, and single or paired cells were often clustered around a single FA particle (on the right). Also, HA cells were closer to confluency than FA cells at day 7.

Conclusions: The addition of apatite microparticles seems to increase osteogenic cell differentiation during the first 3-5 days. This held especially true for HA particles in ALP activity for osteoblasts and DPSCs, and FA particles in collagen production. However, the addition of microparticles proved to be more of a hindrance after 5 days. BMSCs performed much better overall without the addition of particles when compared to osteoblasts and DPSCs. In the future, different concentrations of HA and FA particles may be explored.

Synthesis and Characterization of Hyaluronic Acid based Hydrogels for Biomedical Applications

Kevin Keith, Benjamin Jacoby, Tyler Youngman.
Clemson University

Statement of Purpose: The purpose of this research was to uncover useful methods for synthesizing biologically functional Hyaluronic Acid (HA) hydrogels. A thorough literature review revealed that very few methods exist to create these hydrogels, and those that do are often incompatible for sustained use in vivo (toxic crosslinker, required highly alkaline environment, etc.). In addition to investigating possible biologically compatible linkage methods, determining the characteristics and behavior of the HA hydrogels were also an important project objective. HA is also an attractive building block for new biocompatible and biodegradable polymers with particularly attractive applications in drug delivery. Chemical modification allows the physicochemical properties and in vivo residence time of HA to be tailored to specific applications while retaining its natural biocompatibility, biodegradability, and lack of immunogenicity.

Methods: Three stock solutions of HA were prepared at 0.5, 1 and 2 w/v%. PEGDA in weight rations of 1:5, 1:10, 1:15 and 1:20 were then added to the three pre-made HA solutions, and vortexed mixed together for 3-5 minutes. HA leaching was characterized using High Performance Liquid Chromatography (HPLC). Synthesized hydrogels discs were placed in 20 mL of water at room temperature, and 0.5 mL of surrounding water was collected at days 1, 3, 7, 10 and 14. Swelling ratio for each PEGDA sIPN hydrogel was determined comparison of the sIPN dry mass with its wet mass. Synthesized hydrogels were lyophilized for 72 h, after which each sample was weighed so as to obtain the dry mass. The samples were then placed in water at room temperature and left to sit for periods of 1, 3, 5 and 7 days. Finally, rheological properties of each hydrogel formed were characterized through the use of a photo-rheometer, which was able to illustrate the crosslinking process as a function of UV exposure. The state of crosslinking was characterized using the storage modulus.

Results: HPLC data for day 1 and day 14 are illustrated below in Figure 1. It can be concluded that HA leaching does indeed occur, and that it increases with time.
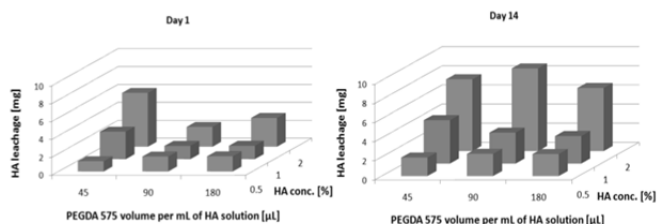

Figure 1 HA release after: (a) day 1, and (b) and at day 14 (right), using PEGDA 575

Results indicate that the initial HA concentration is the driving force behind HA release, whereas the PEGDA content plays no statistically significant role. From a HA percentage release perspective, significantly more is released for an initial HA concentration of 0.5 % than for the 1 and 2 % HA solutions. The influence of PEGDA may however be significant in the longer term, as one might expect that the PEGDA content, and thus density of the PEG network, plays a role in moderating HA release. The swelling ratios after 24 h and 7 days are show in Figure 2, and are seen to vary between 5 and 20. This may be accounted for by the previous HPLC measurements, which concluded that 30-50 % of the total HA may leach out by day 7. Accordingly, regardless of the amount of HA, a higher PEGDA content implies lower swelling ratio, as expected due to the higher crosslinking density.

Figure 2 Swelling ratio after (a) day 1, and (b) at day 7, using PEGDA 575 (significant).
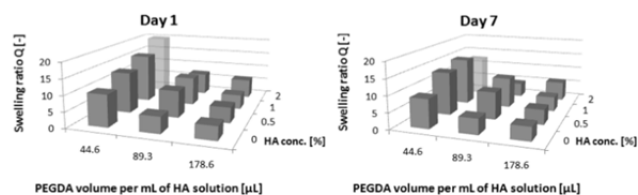
Conclusions: The objectives of this project were to synthesize and characterize novel hyaluronic acid (HA) based hydrogels for potential biomedical applications. The focus of the study was to determine the influence of HA and PEGDA content on HA release, swelling and rheological properties of the hydrogel. Results indicated that there was no statistically significant difference between the PEGDA 575 and 700 hydrogels, and that hydrogels with a greater initial HA content shall release more HA in absolute terms during the same period of time. In percentage release terms, nonetheless, the initial concentration does play in governing the release mechanism. The swelling behavior of the hydrogels was proved to be governed only by the PEGDA content, as expected since it is the PEDGA that forms the hydrogel network.

References:

J. Burdick and G.D. Prestwich, "Hyaluronic acid hydrogels for biomedical applications.," Advanced materials (Deerfield Beach, Fla.), vol. 23, Mar. 2011, pp. 41- 56.

J. Kopecek, "Hydrogel Biomaterials: A Smart Future?," Biomaterials, vol. 28, Jul. 2007, pp. 5185-5192.

The Effect of Proton-Source Radiation on the Wear Properties of Ultra High Molecular Weight Polyethylene

Jonathon Ball[1], Kirk Norasak[1], Eric Lucas[1], Tri Kieu[1], John J. DesJardins[1]
[1]Department of Bioengineering, Clemson University, Clemson, SC 29634

Statement of Purpose:
Ultra High Molecular Weight Polyethylene (UHMWPE) is a widely used polymer in biomedical applications, including hip and knee joint replacements. It is an ideal material selection for bearing surfaces due to its high abrasion resistance, low friction coefficient, and wear resistance.[1-3] UHMWPE is also a commonly used shielding material in aerospace applications, where it is subjected to proton-source radiation from solar events and galactic cosmic rays.[4] While the use of gamma radiation in sterilization of UHMWPE has been the subject of considerable research, there has been no inquiry into proton-source radiation. It is hypothesized that proton-source radiation will have a significant effect on the wear properties of the UHMWPE.

Methods:
Medical grade GUR1020 UHWMPE was machined into pins for standard pin-on-disk wear testing (OrthoPOD, AMTI, Watertown, MA). Pins had an 8mm diameter and a 60 degree tapered tip terminating at a 3mm diameter flat face. Test specimens were exposed to clinically and space relevant proton radiation doses of 0 Gy and 35 Gy (Loma Linda Proton Therapy Center, Loma Linda, CA), and 8 pins were tested from each dose. Pins were subjected to a circular wear pattern at 6MPa for 40km with a constant velocity of 1000 Hertz, and examined for surface roughness (Wyko NT-2000, Veeco Instruments, Plainview, NY) and mass loss at 10km intervals. The disks used in the experiment were polished to an average surface roughness of 700 nm. Bovine Serum was used as a lubricant with the addition of 0.2% Sodium Azide. Deionized water was added to the lubricant every 8 hours to maintain a proper concentration.

Results:
Wear for the 0Gy specimens can be seen in Table 1. Surface roughness values from both the pins and the disks are shown in table 2 and 3 respectively. Results for the 35Gy dose samples are being processed. Once complete, differences will be analyzed for statistical significance.

Table 1: Mass (g) of 0 Gy UHMWPE Pins Before, During, and After Completion of Wear Test

Pin #	0 km	20 km	40km	Wear
1	1.4787	1.4782	1.4784	0.0003
2	1.4757	1.4739	1.4732	0.0026
3	1.4870	1.4862	1.4857	0.0013
4	1.4799	1.4783	1.4774	0.0025
5	1.4905	1.4897	1.4891	0.0014
6	1.4782	1.4780	1.4779	0.0004
7	1.4856	1.4856	1.4856	0.0000
8	1.4783	1.4782	1.4784	0.0000

Table 2: Average Surface Roughness of 1020 UHMWPE 0Gy

Pin #	Avg Ra	Avg Rz	Avg Rt	Avg Rq
1	1352.48	11789.86	13487.29	1693.36
2	2923.13	19801.55	22021.53	3547.32
3	2501.26	15245.34	16961.38	2949.43
4	2234.19	16607.05	17500.53	2786.95
5	2689.96	18711.36	19567.34	3271.17
6	1329.45	9760.12	10711.64	1664.54
7	3467.57	16904.76	17602.88	4016.19
8	1979.32	13539.00	14874.68	2394.37

Table 3: Average Surface Roughness of 316L Stainless Steel Disks

Puck	Rz	Ra	Rq	Rt
Avg. 1	1320.65	66.43	90.68	1839.37
Std. Dev. 1	318.86	9.33	12.60	872.78
Avg. 2	1909.82	66.21	99.25	2903.16
Std. Dev. 2	389.06	5.45	8.74	887.75
Avg. 3	1251.90	72.31	99.64	1577.58
Std. Dev. 3	234.42	9.55	14.61	346.84
Avg. 4	1421.26	71.76	103.26	1832.37
Std. Dev. 4	353.70	8.87	18.31	600.27
Avg. 5	1344.88	69.80	96.98	1843.96
Std. Dev. 5	373.07	7.64	13.12	810.27
Avg. 6	1739.73	69.85	105.20	2448.43
Std. Dev. 6	362.25	9.64	17.06	523.47

Conclusions:
Conclusions are contingent upon finalization of results.

References: (1) Archodoulaki, V. *J Appl Polym Sci* 1875:84, 120. ; (2) Burroughs, B. *Wear* **2006**, *261*, 1277-1284. ; (3) Costa, L. *Polym. Degrad. Stab.* **2009**, *94*, 1542-1547. ; (4) Zhong, W. *Composites Sci. Technol.* **2009**, *69*, 2093-7.

Implant Alignment Reproducibility in a Reverse Shoulder Arthroplasty Micromotion Study

Wooten D. Simpson III[1], Andrew D. Bries[2], Stephan J. Tolan[2], Melinda Harman[1],
Richard J. Hawkins[2], John D. DesJardins[1]

[1]Department of Bioengineering, Clemson University, 29634,
[2]Steadman Hawkins Clinic of the Carolinas, Greenville, SC, 29615

Statement of Purpose: As the world's population quickly ages joint replacements are becoming more necessary and, as a result, shoulder replacements are becoming more commonplace. The standard shoulder arthroplasty has proven to be successful in patients lacking significant rotator cuff damage[2]. However, in patients that exhibit rotator cuff deficiency, reverse shoulder arthroplasty (RSA) has been more successful[2,3,4]. Reverse anatomy shoulder implants are a relatively new implant design increasing in demand and there has not been sufficient research performed on many aspects of the implants[1,4]. Early range of motion rehabilitation following reverse shoulder arthroplasty is encouraged, but it has the potential to subject the bone-implant interface of some RSA designs to detrimental micromotion. Loosening of the glenoid component is one of the most common complications of reverse shoulder designs[3]. There are many factors that can affect the initial fixation of the glenoid baseplate: configuration of the baseplate screws (position, size, number, direction, locking ability), central screw design, initial inclination[3]. This abstract will assess the initial inclination of one RSA design.

Methods: In this study, a novel dynamic testing platform was designed, and the initial pre-testing alignment of a set of RSA implants was investigated prior to micromotion testing. A new testing fixture was designed; enhancing the ASTM 2028 standard to include dynamic cyclic 0-55° ab/adduction in combination with compressive shoulder joint compression of 460N, followed by conventional implant micromotion analysis (figure 2). Three RSA designs will be investigated. To date, 5 DJO Surgical (Reverse®, Austin, TX) RSA genoid conenenets have been implanted as per surgical specifications into mechanically equivalent osteopenic anatomical Sawbones scapula (4th Generation Custom, Model 4313 Large, Pacific Labs, Vashon Island, WA). Pre-testing bi-planar x-ray alignment goniometric analysis was conducted to determine initial implant baseplate alignment with respect to glenoid fossa anatomical references (figure 1).
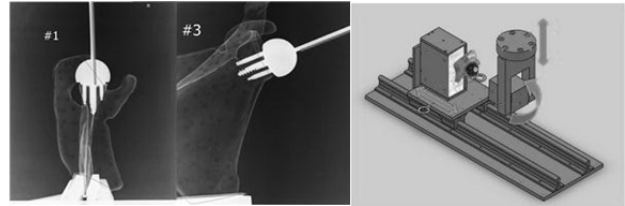

Figure 1 (left) Frontal/transverse plane x-rays of RSA implant alignment in sawbone scapulas. Figure 2 (right) Enhanced ASTM2028 micromotion testing platform showing intended component movement
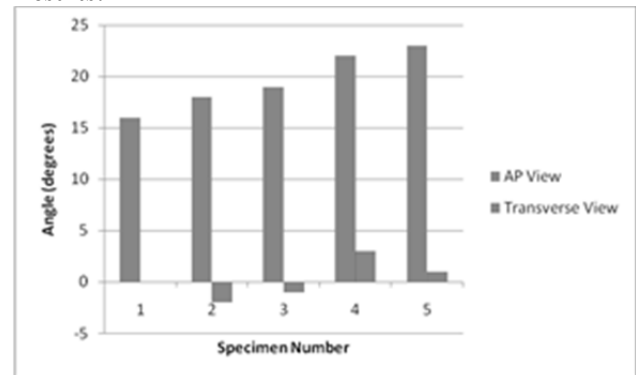
Results:

Figure 3. Graph of implant alignment measurements taken for each DJO speciman from the AP and transverse views.

Results show that average (±1 StDev) frontal plane baseplate inferior inclination was 19.6±2.8° (range 16-23, from an ideal of 15°). Average transverse plane anterior tilt was 0.2±1.3° (range -2 to 3°, from an ideal of 0°).

Conclusions: Initial alignment results between implant designs will be correlated with future micromotion data. It is hoped that the use of mechanically equivalent anatomical scapula in this work, combined with the addition of cyclic dynamic anatomical articulations will enhance the validity of this micromotion study.

References: 1. Harman M, Frankle, M, et al. *J Shoulder Elbow Surg.* 2005 Jan-Feb 14(1 Suppl S):162S-167S.
2. Virani, Nazeem A, Harman, Melinda, et al. *J Shoulder Elbow Surgery.* 2008, Vol 17: 509-521.
3. Poon PC, Chou J, Young D, et al.. *British Elbow and Shoulder Society.* 2010, Vol 2: 94-99.
4. Guitierrez S, Greiwe RM, Frankle MA, Siegal S, Lee III WE. *J of Shoulder and Elbow Surgery.* 2007, May/Jun

Re-Engineering Medical Training Simulators - CLiVE

Elizabeth Burghardt, Melissa Dunphy, Kaitlin Grove, Nadine Luedicke, Molly Townsend, Elizabeth Tumblin, George Fercana, Delphine Dean, PhD, Jiro Nagatomi, PhD

Clemson University

Statement of Purpose: When a patient requires a large influx of a drug, doctors need to insert a large catheter into a major vein in the neck using a technique known as central venous catheterization (CVC). In order to learn this life saving medical procedure, adequate training methods are required. Unfortunately, the best method for learning this procedure is the often using a live patient. Even for skilled practitioners, CVC can lead to fatalities if the needle misses by even a few millimeters, puncturing a lung or a major artery in the thoracic cavity. Use of a live patient by an unpracticed trainee places the patient in an even more precarious situation. As an alternative, training simulators have been designed to allow safe practice of this procedure. Unfortunately, those simulators currently on the market lack the appropriate bony landmarks and rotatable head, are difficult to manipulate, or are extremely expensive – reducing their usefulness. In addition, most current simulators cannot simulate the valsalva maneuver or adequately simulate the echotexture of human skin for ultrasound – two crucial techniques used to locate veins. Our team has worked to design a novel CVC training simulator using a modified gel insert that includes all necessary anatomical landmarks and vasculature as well as a manikin with a fully rotatable head. Our simulator design can also provide useful ultrasound images to the technician at a lower cost than previous simulators.

Methods: In order to design a novel simulator, a pre-market survey was conducted. This survey found that current CVC simulators lacked a rotatable head, accurate vasculature and bony landmarks, and the ability to allow the technician to utilize ultrasound technology. A manikin with a rotatable head was obtained and a cut was made into the chest to allow a custom designed puncture pad to be fit. A reverse mold was then made to create the shape of the puncture pad, with accurate contours of the human chest. A puncture pad analogue was designed utilizing a modified ballistics gel with a cross linking agent in order to increase mechanical strength. Anatomically correct bones were cast in silicone to provide a reverse template for injection molding. Bone materials were then tested for hardness and similarity to standard bones. In order to design a realistic vasculature system, different types of tubing were tested to verify that the material could provide realistic pulsatile flow in arteries and increase the diameter of veins, thus simulating blood flow, as seen in **Figure 1**.
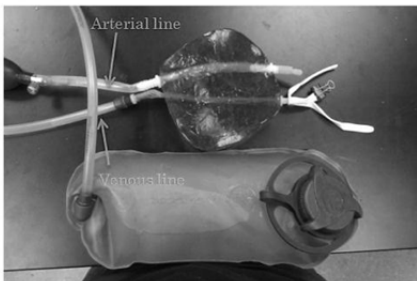

Figure 2: Small scale model of vascular system.

It was also necessary to design a workstation for our simulator in order to remove the need for a hospital bed. To do so, a platform was designed and machined from polycarbonate. This design allowed the simulator to rise into the trendleburg position, with the head 10-15° below the feet, as seen in **Figure 2**.

Figure 3: Simulator platform in trendlenburg position.

Results: After testing multiple ratios of gelatin and cross linking agent, we determined a formula that takes into account the ratios of components for the gelatin in the puncture pad: the gelatin, an antifungal agent, water, and cross linking agent. Initially, the inclusions would not remain in place and alternative methods were needed, it was found that by placing the bones into the mold for the puncture pad using magnets, we could adequately secure the inclusions while pouring the gelatin. For the bony landmarks, it was decided to include the clavicle, the first and second ribs, as well as the sternum. These bones were cast using the Amazing Casting Solution©. For the vasculature, custom tubing was utilized for arteries due to thin walls and the necessary ability to simulate pulsatile flow. Thin latex was selected to simulate veins, as it significantly expanded when the simulator is placed into the trendleburg position,

The platform design was found to be successful. The simulator accurately simulated vein dilation when the platform was adjusted to the appropriate angle. Also, the platform design significantly reduced the amount of water leaking onto the surface supporting our platform, thus eliminating the issue of workspace staining and messiness that is associated with current simulator models.

Conclusions: The Central Line Vascular Emulator (CLiVE) was found to be more cost effective and more clinically accurate than those simulators currently on the market. Our simulator can accurately simulate the necessary steps of CVC, while also providing accurate ultrasound images of skin. Also, our platform significantly reduces clean up after performing this procedure and the puncture pad is of low enough cost that it can be easily replaced. It was also found that our replacement puncture pads can be premade and stored for an extended period of time without degradation. It was found that the cost of a full simulator, including labor costs and a profit margin would be approximately $1000, significantly lower than the $1300 average cost of a CVC simulator on the market today. CLiVE is a worthwhile market investment and also an accurate simulator for those medical professionals seeking to reduce risks for patients.

Biomechanical Testing of PRP Augmented Microfracture in Cartilage Regeneration in a Lapine Model

Miles C. Ware[1], Juan J. Rodrigo[2], Shea A. Bielby[1], Ashley B. Anderson[3], Douglas J. Wyland[2], John D. DesJardins[1]

1. Clemson University Bioengineering, 2. Steadman Hawkins Clinic of the Carolinas, 3. The Hawkins Foundation

Statement of Purpose: With total joint replacement surgeries becoming increasingly common, less invasive surgeries such as microfracture are gaining in popularity in an attempt to regenerate areas of diseased or damaged articular cartilage. This study assesses the efficacy of using platelet rich plasma (PRP) soaked synovial sponges in concert with microfracture to enhance the quality and coverage of neo-generated cartilage.

Methods: Thirteen male New Zealand white rabbits (mean age 13.5 mos.) underwent full thickness patellar groove defects in the left knee and subsequent treatment with PRP augmented microfracture (with right knees serving as controls). After sacrifice at four months, microindentation mechanical testing of the neo-cartilage was performed using a 1mm steel indenter and a 0.7 N/min ramp indentation load. A 15x2mm indentation grid was performed along the patellar groove with 1mm spacings. Elastic modulus (E) was assessed by fitting the upper 20th percentile of the load vs. displacement curve to the Hertz model for a spherical indenter tip.

Results: Analysis showed that the articular cartilage control had an average E of 7.60±1.45 MPa while that of the regenerated cartilage area was 6.13±1.98 MPa (p=0.0611, student's t-test, α=0.05). Using NIH ImageJ software on post-operative photographs, it was determined that the neo-cartilage obtained a 65.35%±10.80% fill of the total defect area.

Conclusions: The new microindentation testing matrix method was proven effective in assessing the distributed mechanical properties of the cartilage, as well as differentiating between areas of neo-cartilage and bone. With these encouraging results, further research will need to be done using both stem cells and cytokines, with traditional microfracture serving as controls to determine the efficacy of microfracture augmentation in improving regrowth response.
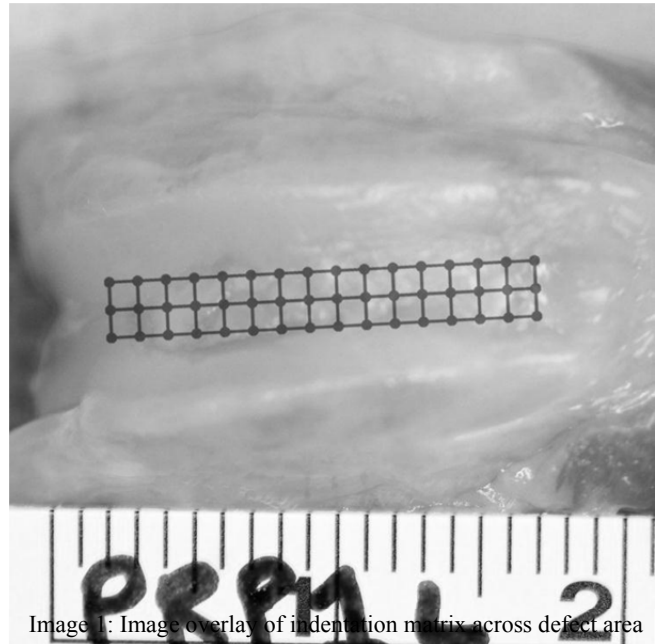

Image 1: Image overlay of indentation matrix across defect area

Society For
Biomaterials

CLEMSON
BIOENGINEERING

BioMEDS
Biomedical Engineering Development Society

CBS
CLEMSON BIOENGINEERING SOCIETY

BioMATERIALS DAY

Clemson University - October 1, 2011 - Madren Center - Clemson, SC

Graduate Student Abstracts

Surface Damage Classification and Training Method for Evaluating Metal Bearing Surfaces of Retrieved Femoral Components

+[1]Alvarez, E; [1]Harman, MK; [1]DesJardins, JD
+[1]Dept. of Bioengineering, Clemson University, Clemson, SC, USA
ealvare@clemson.edu

SIGNIFICANCE: The Femoral Damage Mode Atlas is an illustrative reference tool for surface damage analysis of metal knee prostheses, and can be applied to the assessment of in-vitro wear testing and retrieved components. In this study, the training of new observers using the damage atlas successfully increased the accuracy and inter-observer reliability of surface damage mode assessment results.

INTRODUCTION: Implant retrieval analysis is a valuable assessment tool that assists in the identification of clinical and implant failure modes and material performance that can directly affect implant longevity. Limited retrieval data suggests that scratched metal femoral components can significantly accelerate polyethylene bearing counterface wear.[2-5] However, few retrieval studies report the in vivo femoral component surface damage [1,2] and there are no standard guidelines for analyzing the surface condition of retrieved femoral components.

The objectives of this study were: 1) to develop a new illustrative reference guide (Damage Mode Atlas) to aid in the identification of damage modes on retrieved femoral knee components; and 2) to assess the experimental validity of using this Atlas as a training tool for damage mode assessment.

METHODS: Fifty three femoral knee components were selected from retrieved revision knee arthroplasty specimens in the IRB approved Clemson University Retrieval of Explants Program and Registry in Orthopaedics (CU-REPRO). The specimens included medical grade titanium (n=8), cobalt chrome (n=43) and oxidized zirconium (n=2). The bearings were fixed with formalin (10%) and cleaned according to ASTM-F1715. One researcher (EA) experienced in characterizing surface damage modes identified and marked 130 specific damaged regions across these articular surfaces (approx. 3-4 per implant). The assessment was based on visual identification techniques using the unaided eye and a stereomicroscope at 12x magnification under uniform lighting conditions (model K400P, Motic Inc., Xiamen, China). These damaged regions included eight damage modes with the following frequency: linear abrasion (25%), circular abrasion (7%), pitting (6%), scratching (20%), tool damage (12%), dulling (6%), adhesive wear/material transfer (16%), fracture (1%) and no damage (9%). An illustrative reference guide (Damage Mode Atlas, figure 1) was compiled using digital images (1392x1040 pixel resolution) of each mode and their respective definitions derived from published literature. [1,2, 5-9]

New observers (n=4) were first trained using 'Written Training', in which the observers were provided the written definitions of each damage mode than then asked to review and score the 130 specific damage areas previously selected. Following this, each observer then received 'Atlas Training', in which the written definitions, the illustrative Damage Atlas and a table of characteristics features that described scale, spatial density and reflectivity of each mode under uniform lightning and magnification were provided, and then repeated the assessment of the 130 specific damage areas. Statistical analysis was performed to compare the effectiveness of the two training sessions (Written Training versus Atlas Training). Observer accuracy after each training session was determined as the proportion of correctly identified regions in the two matched pair sessions (McNemar's test): Inter-observer reliability was assessed using an intra-class correlation coefficient (Fleiss' κ). Total time required to assess the 130 regions was recorded for each observer.

RESULTS: The use of the Damage Atlas training statistically increased the accuracy of damage mode identification and reduced the overall time to complete the evaluation. Each observer had a significantly greater proportion of correctly identified damage modes in the Atlas Training session compared to the Written Training session alone (McNemar's Test, $p<0.05$ for each observer). The average for all observers increased from $76\% \pm 6\%$ (range, 70% to 82%) after the Written Training to $90\% \pm 1\%$ (range, 89% to 90%) after the Atlas Training. All four observers correctly identified 87/130 (67%) regions after Written Training session ($\kappa=0.72$) and 105/130 (81%) regions after the Atlas training. The time required to complete the inspection of all regions was reduced by 33%, from 202 ± 37 minutes to 135 ± 6 minutes ($\kappa=0.84$).
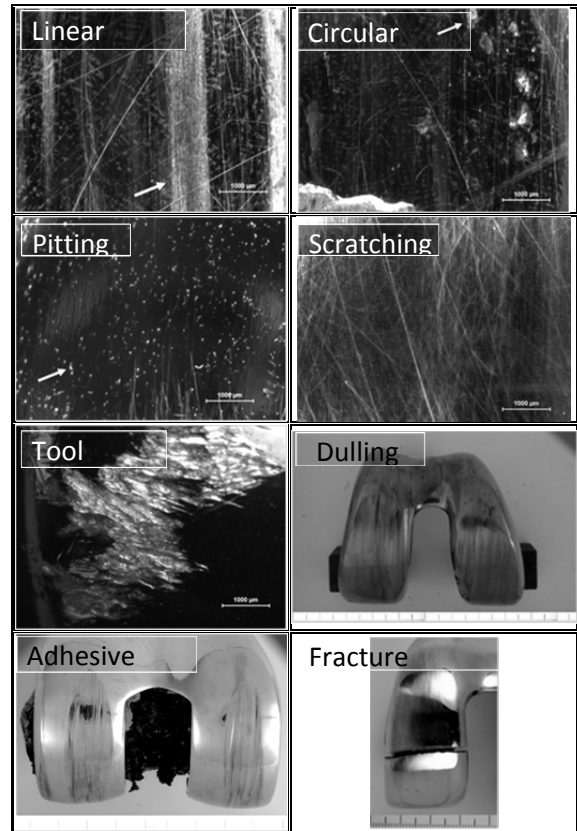

Figure 1: Representative images of the Damage Atlas developed for the accurate assessment of femoral component surface damage.

DISCUSSION: Retrieved prostheses are a unique source of information that provide invaluable insight into the surface damage that occurs with in vitro and in vivo function. This study assessed the importance of providing uniform definitions and representative illustrations of the different damage modes to assist in the accurate analysis of retrieved metallic femoral components. The Damage Atlas included definitions, visual descriptions, and uniformly calibrated images of prevalent damage modes that are commonly seen on the three primary alloys used in femoral prostheses. Acquiring images of the unique damage modes under uniform lighting conditions and magnification allowed relative size and difference in reflectivity to be distinguished.

Results show that training the observers to initially recognize the alloy composition of the femoral components and to appreciate the typical appearance of non-damaged surfaces aided the recognition of different modes that were specific to each alloy. It was important for the observers to start the assessment with gross (macro) observations of the damage and then proceed to the microscopic view. This was especially useful in cases with adhesive wear and in distinguishing between abrasive damage and scratch damage.

REFERENCES:
[1] Heyse et al., J Arthroplast, 2011. [2] Que et al., J. Biomed Mater Res, 2000. [3] Dowson et al., Wear, 1987. [4] Levesque, et al., Proc. ORS, 1998. [5] Muratoglu et al., J. Arthoplast., 2004. [6] Budinski et al., Wear, 1991. [7] Lombardi, et al., JBJS-Am., 1988. [8] McKellop, et al. ASTM STP 1272. 1996. [9] Rimnac, et al., Mater. Charact, 1991.

Computer Aided Image Analysis of Retrieved
Metallic Femoral Knee Implant Surface Damage

Breitmeier, J.[1,2] Kwartowitz, D.[1] Gowdy, J.[2] DesJardins, J.D. [1]

1. Department of Bioengineering, 2. Department of Electrical and Computer Engineering
Clemson University, Clemson, S

Introduction:

Devices that are retrieved from patients offer enormous potential to be used to characterize the strengths and weaknesses of the implant's design and biomaterial performance. Studying the surface damage in recovered metallic components gives insight on the characteristics of usage, while granting an *in vivo* perspective of the durability and longevity of the specific alloys used. With modern devices, the amount of damage in metallic components can be minimal, usually on a microscopic scale, requiring the use of tools like surface contacting stylus and optical profilometers.

This study seeks to refine the analysis of collected surface roughness data and provide a uniform assessment method for the surface damage of devices. Current surface roughness techniques collect many small images along the polished, curved surfaces of these devices. Software then characterizes these images with measures of roughness which are usually averages across the entire image. Roughness averaging has a limited perspective, which ignores valuable information on the size and depth of damage, as well as possible direction and repetition of scratches.

Methods:

In the current study, image detection algorithms and other pattern recognition methods have been applied to find instances of abrasion, or scratching in the image. Initially the images are being implemented in the MATLAB environment using edge detection to find instances of damage. Automated scratch damage detection is being implemented using edge detection and Hough transforms to locate and piece together scratch instances.

Results:

The Hough transform is an iterative voting system where higher intensity indicates more points on a line, figure 1. The current work allows for automated detection of linear scratches, and local assessment once found, figure 2.
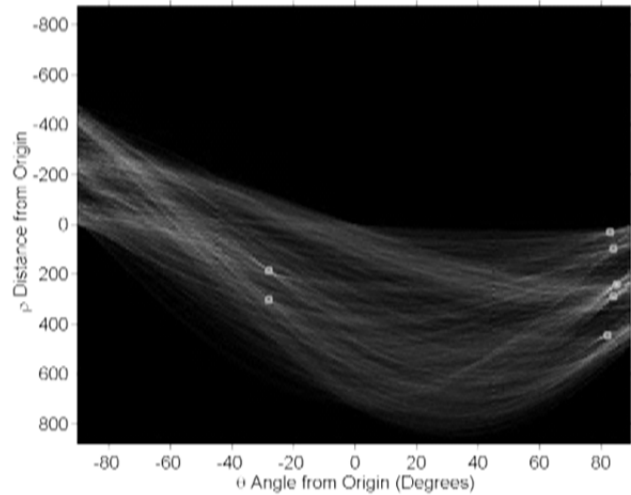

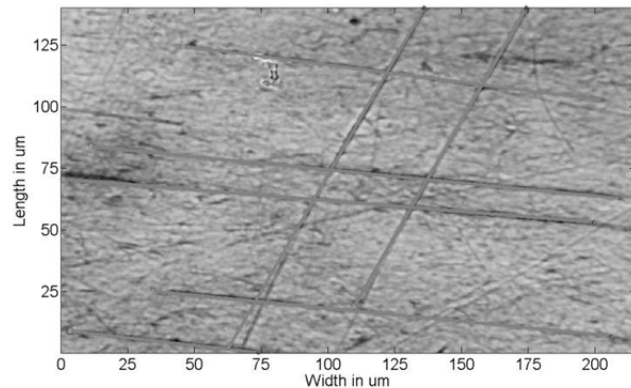Figure 1: Hough Transform of Detected Edges in Image, Intensity Peaks are in Green

Figure 2: Image of Recovered Implant with Automatically Detected Hough Lines in Green

Conclusion:

Future work will determine if these automated methods of quantifying the surface damage in recovered metallic components will yield greater insight into the characteristics of *in vivo* use, and assist in the development of more durable implants for greater implant longevity.

Preparation of Absorbable Microrod Systems for Regulated Delivery of Ocular Therapeutic Agents

C. J. Culbreath, J. M. Olbrich, M.S. Taylor, J. T. Corbett
Poly-Med, Inc., Anderson, SC

Statement of Purpose: Absorbable polymeric materials are increasingly common in surgical implants and other clinical applications. Also prevalent now is the incorporation of drugs with polymers to localize and regulate the therapeutic treatment. Ocular drug delivery devices, in many cases, are extremely small due to their implantation via small gauge needles into the vitreous humor. This abstract identifies a novel method to produce an extremely small drug loaded microrod, 0.144 mm3 nominal volume, and examines its characteristics. To this end, a study was performed to explore the *in vitro* response of a commercially available absorbable polymer, RG 752 S (Boehringer Ingelheim, Ingelheim am Rhein). The copolymer consists of 75% polylactide and 25% polyglycolide (PLGA) and the utilized drug was an ocular therapeutic agent. The material properties observed in this study included radial swelling and drug release rate from the microrod.

Methods: The polymer/drug mixture was combined by multiple methods including grinding and solvent casting of a film. Microrods were molded by means of six ~350 μm diameter channels in a specially designed mold. The drug loaded polymer was heated until flowable and drawn into the mold under vacuum assist. Following cooling, the mold was opened and the prepared rods were removed. Selected samples were retained in the mold and annealed at 50°C for 75 minutes before removal. Yet another group of samples were spray coated after removal with the same RG 752 S polymer. The coating polymer was dissolved and aerosol sprayed. The rods were placed into a coating apparatus with wire filters above and below. The coating solution was sprayed in a small burst. After the spray coating, the rods were allowed to dry and then removed from the apparatus. This process was continued until the coating appeared to be evenly applied over the entirety of each rod. The mold and method were also used to make microrods using Poly-Med novel materials such as BTE1 and H2. The molding produced microrods with an initial diameter of ~350 μm and length 1.5 mm. These samples were examined through a batch *in vitro* release study simulating physiological conditions. Eluents were analyzed for drug concentration via reversed phase HPLC at predetermined time points. At other predetermined time points microscopic pictures were taken of the individual microrods while in the same simulated physiological conditions in order to determine swelling.

Results: The observed diameter increase was >60% for all RG 752 S samples within 33 days of exposure to physiological conditions. Poly-Med novel materials did not relatively exhibit swelling or loss of dimensional stability. See Figure 1.
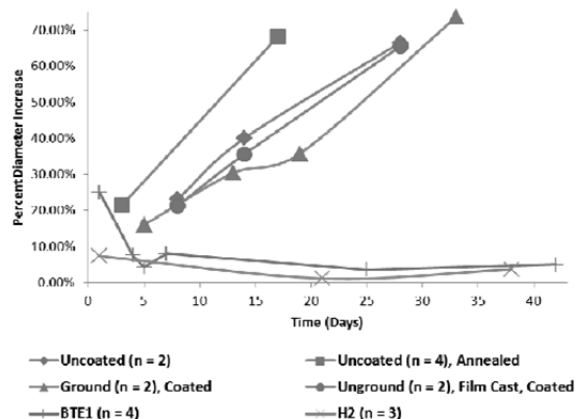

Figure 1: Swelling, Microrod Radial Increase in 7.2 pH Phosphate Buffer, 37°C
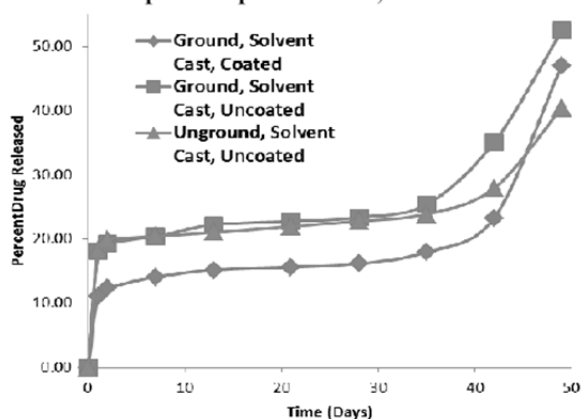
Legend: Uncoated (n = 2); Uncoated (n = 4), Annealed; Ground (n = 2), Coated; Unground (n = 2), Film Cast, Coated; BTE1 (n = 4); H2 (n = 3)

Figure 2: Cumulative Release, Microrods in 7.2 pH Phosphate Buffer, 37°C

Legend: Ground, Solvent Cast, Coated; Ground, Solvent Cast, Uncoated; Unground, Solvent Cast, Uncoated

The coating process resulted in a coating thickness of 8.1 to 13.3 micrometers. The coating demonstrated an ability to help minimize the release burst. See Figure 2.

Conclusions: In spite of the extreme challenges of the small device volume, microrods for use as implantable ocular drug devices, 0.144 mm3 nominal volumes, were constructed successfully with multiple materials, demonstrating the robustness of the methodology. The polymeric microrods made with commercially available materials displayed poor dimensional stability when exposed to *in vitro* conditions. With novel Poly-Med materials the radial stability was maintained. The microrods were found capable of regulated release that was even further modulated via the coating process. A method to make the rods is now defined. Future work should include testing additional materials and processing methods. The end goal is a dimensionally stable device that releases drug in a regulated manner with minimal initial burst.

Creation of a Novel Static Compression Chamber for Biomechanical Testing of Dental Pulp Stem Cells

Matthew Cupelli, Delphine Dean.
Department of Bioengineering, Clemson University, Clemson, SC.

Statement of Purpose: There are forces in the body that are constantly pushing and pulling on our bones and teeth. Wolff's Law says that bones will adapt to the loads applied to them. If the forces applied to a cell can impact the growth patterns, this knowledge could be used for applications in tissue engineering. The aim of my research project is to determine the effect of compression on dental pulp stem cells. It is known that cartilage cells respond differently (express different levels of proteins) when a load is applied to them, as opposed to being allowed to freely swell.[1] Cartilage has been tested because it is also continually loaded and unloaded with forces. However, dental pulp stem cells have not been tested to see the effects of compression. The first step in the process of testing the response of stem cells to compression was to build a compression chamber.

Methods: To create a static compression chamber, a custom cell culture dish needed to be fabricated. A computer model was designed on Solidworks and taken to the Clemson Machining and Technical Services shop to fabricate. The custom device was designed to fit onto the top of a standard 6-well cell culture dish. Following fabrication of the chamber, a protocol for forming gels to place under compression was needed. Using past literature, a protocol was formed and tested. In a conical tube, 800 µL of type 1 collagen at a concentration of 1mg/mL was mixed with 100 µL of pH 9 HEPES and 100 µL of 10X MEM. 60,000 osteoblast cells were added to the mixture and it was transferred onto glass coverslips in the 6-well culture dish at 165 µL/coverslip and allowed to incubate at 37°C and 5% CO_2 for 30 minutes. Lastly, to allow for confined compression studies, cylindrical molds needed to be formed to act as a collagen gel chamber. A Sylgard 184 Silicone Elastomer kit was used along with 12mm cylinders to form hollow cylinders inside a stiff elastomer material. An example of the resulting material can be seen in Figure 1.
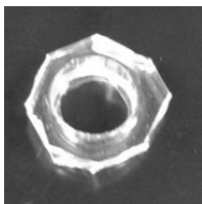

Figure 1: The elastomer chamber to hold collagen gels

Results: The static compression chamber fabricated by the machine shop was designed to have a clearance fit on top of the cell culture dish and it fit well. The custom top was made of 316L Medical Grade Stainless Steel, and it has a mass of 632 grams. Considering that there are 6 cylinders protruding into the cell culture plate, and each cylinder is 12mm in diameter, a pressure of 0.93 g/mm^2 will be applied to the collagen gels.

The protocol for the polymerization of collagen gels was successful. However, the gels spread in different patterns on the coverslips.

The procedure for fabricating the hollow molds from the elastomeric material was also successful. Figure 2 shows pictures of the parts of the compression chamber.
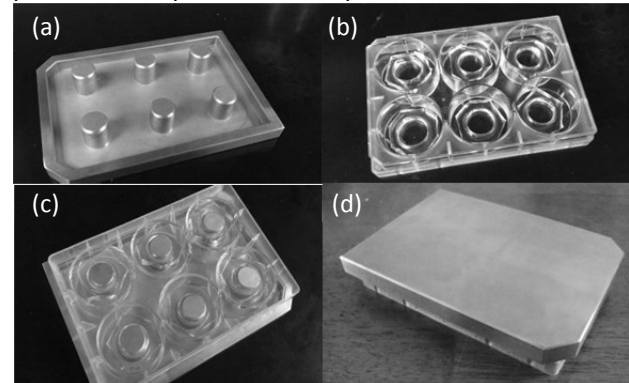

Figure 2: (a) a view of the bottom of the custom cell culture dish top. (b) the cell culture dish with the elastomer molds inside. Also, view from the bottom (c) and top (d) of the assembled static compression chamber.

Conclusions: All components of the cell compression chamber work as designed, and are currently being used for testing. No data has been collected yet. To reduce to spreading of the collagen gel, all gels have been formed inside the hollow elastomer chambers. For confined compression, the chambers will stay in place, but for unconfined compression they will be removed before the gels are compressed.

The next steps are to culture dental pulp stem cells and grow them in the collagen gels inside the compression chamber. Culture times of 1, 4, 7, 14, and 21 days will be observed under different loading conditions. Different loading frequencies will be used (time on vs. time off) along with different weight loads. Alkaline phosphatase and BCA assays will be performed on the samples at each time point and some will be fixed and stained for confocal imaging. Also, Western blotting will be done if time allows. Also, a duplicate compression chamber will be fabricated using an acrylic polymer to replace stainless steel. This change in materials will reduce the base weight of the custom device and allow for more variability in testing weights.

Overall, a novel static compression chamber to test dental pulp stem cells has been fabricated and will be used over the next year to determine the growth patterns of the cells under different compressive conditions.

References:
[1] G. Nugent, et al. "Static and dynamic compression regulate cartilage metabolism of proteoglycan 4." *Biorheology*. 43.3 (2006): 191-200. Print

Characterizing Mechanical Heterogeneity in Vascular Smooth Muscle Cells

Sandra Deitch, Delphine Dean
Clemson University

Statement of Purpose: Most tissue-level mechanical models assume homogeneous mechanical properties within a single cell type. However, measurements of cellular mechanical properties show large variability in whole-cell mechanical properties between cells from a single population. This heterogeneity has been observed in many cell populations and with several measurement techniques but the sources are not yet fully understood [1]. Cell mechanical properties are directly related to the composition and organization of the cytoskeleton, which is physically coupled to neighboring cells through adherens junctions and to underlying matrix scaffolds through focal adhesion complexes. As such, we believe that this high level of heterogeneity can be attributed to varying local microenvironment conditions throughout the sample. To test this hypothesis, vascular smooth muscle cells (VSMCs) were cultured under several conditions that limited their microenvironment variability (aligned matrices, inhibited cell-cell and cell-matrix interactions) prior to measuring their mechanical properties. To more closely mimic the native microenvironment, experiments were replicated on gels and under tension conditions.

Methods: Substrates (glass slides, gels (10-75 kPa), flexible elastomer membranes) were coated with thin layers of 1 mg/ml solutions of collagen and fibronectin in aligned (inkjet printer) and unaligned orientations. Vascular smooth muscle cells (P5-P8) were seeded on the coverslips in a subconfluent layer. For the test groups, the media was supplemented with 50 µg/ml anti-N-cadherin, 50 µg/ml anti-integrin β1, or 50 µg/ml of both antibodies to block cell-cell and/or cell-matrix interactions. On day 5 in culture, AFM (Asylum Research MFP-3D) cytoindentation experiments were performed using a 5 µm diameter borosilicate spherical-tipped probe. Twenty cells on each sample were indented 5 times to ~1 µm depth at 1 µm/sec. The elastic modulus was estimated by fitting the Hertz model to the first 300 nm of indentation. Each cell was also subjected to two 1 µm step indentation and 60 second hold (stress relaxation) experiments. The Quasilinear Viscoelastic Model (QLV) was fit to the relaxation data to give a measure of the percentage of relaxation during the hold. Fluorescence imaging was used to confirm antibody blocking and to visualize the cytoskeletal arrangement within the cells.

Results: The VSMCs on aligned matrices were stiffer than those on unaligned matrices, but there was no significant change in the overall level of heterogeneity within each sample. For samples with antibodies in the media (blocking cell-cell and cell-matrix interactions), the cellular elastic modulus measures decreased and the percentage relaxation measures increased compared to the control samples (Figure 1). The cell-to-cell variation in mechanical properties remained high for the control cells (average cell-to-cell coefficient of variation (COV) = 116%) and decreased under the blocking conditions (average cell-to-cell COV = 57%). The cells with antibody conditions also appeared more synthetic than the control samples, which contained both contractile and synthetic cells (Figure 2). By limiting the cellular interactions, the microenvironment variability within the sample decreased and, in turn, the cells exhibited decreased heterogeneity in both their phenotype and their mechanical properties.
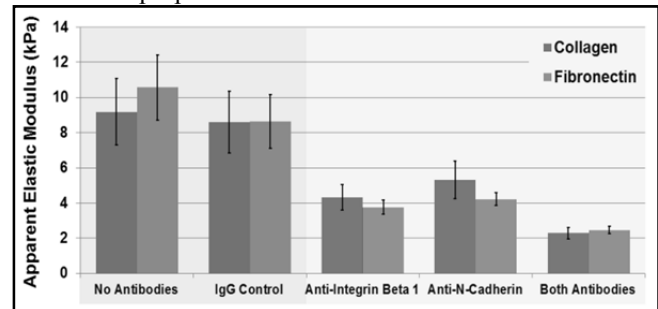

Figure 1. Apparent elastic moduli of day 5 VSMCs on unaligned collagen and fibronectin (glass substrates) with different media conditions. Data presented as mean ± standard error. Blocking cell-cell (N-cadherin) and cell-matrix (integrin β1) interactions decreased the elastic moduli of the cells and decreased the heterogeneity among cells from each sample (smaller error bars).
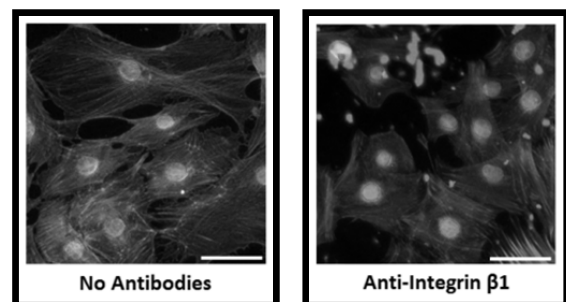

Figure 2. Day 5 VSMCs on unaligned collagen with regular and anti-integrin β1 media conditions. Cells are stained for nuclei (blue), microtubules (red), and actin (green). Under regular media conditions, cells exhibit both contractile and synthetic phenotypes. Under antibody media conditions, cells are generally more synthetic.

Conclusions: The reduction in mechanical heterogeneity among cells under blocking conditions supports our hypothesis that microenvironment variability is to blame for the heterogeneity that is observed in mechanical properties among cells from a single population. Researchers may use these results to consider heterogeneity in the cellular microenvironment in vivo, especially in disease conditions where there is often elevated disorganization, and incorporate realistic levels of cellular heterogeneity in tissue-level mechanical models. Such models may help to better understand tissue behavior in both health and disease.

References: [1] Jaasma, MJ. Ann Biomed Engr. 2006;34:759-768.

A Study of the Blast-Induced Brain White Matter Damage and the Associated Diffuse Axonal Injury

Angela Grujicic, Martine LaBerge, Brian P. d'Entremont, Bhaskar Pandurangan, Mica Grujicic.
Clemson University

Statement of Purpose: Blast-induced traumatic brain injury (TBI) is a signature injury of the current military conflicts [1]. Blast-induced TBIs are classified in a number of ways. One of these classifications identifies: penetrating (pTBI, skull penetration/fracture) and closed (cTBI, structural integrity of the skull is maintained). cTBIs can be further classified according to the severity-level as [2]: (a) mild (mTBI); (b) moderate; and (c) severe. Closed mTBIs can be classified as: (a) primary TBI resulting from the propagation and reflection of shock waves produced directly by the blast; (b) secondary TBI caused by the impact of a person's head with an object propelled by the blast; and (c) tertiary TBI caused by the blast-induced propulsion of a person's head and its subsequent impact against a rigid/hard surrounding structure [3,4]. Closed, primary, mTBIs can be further classified based on the nature of the injury as: (a) diffuse axonal injury; (b) contusion; and (c) subdural hemorrhage [5]. Diffuse axonal injuries (DAIs) are the focus of this work and are believed to be caused by blast-induced stretching and shearing of axons and small vessels which, in turn, lead to impaired axonal transport and subsequent focal axonal swelling and eventual disconnection [5]. DAI occurs mostly in areas of white matter (such as in the corpus callosum), with dense axonal packing.

Methods: A Finite Element Analysis was carried out using ABAQUS/Explicit, utilizing a "representative unit cell (RUC)" of a section of regularly hexagonally-packed axons surrounded by ECM. Both axons and ECM were meshed with continuum eight-node first-order reduced integration hexahedron elements and assumed to be isotropic and linear-elastic. The axonal volume fraction was initially set to 53%, and the axonal radius was initially set to .56 μm. Periodic boundary conditions were applied to the boundaries to emulate the existence of surrounding RUCs. The RUC was prescribed a simple exponential decay equation for shock loading, similar to results obtained from previous work:

$$\sigma(t) = \sigma_{level} + \left(\sigma_{peak} - \sigma_{level}\right)e^{-t/\tau_{relax}}$$

Surfaces comprised of four-node quadrilateral surface elements were made along the axon/ECM interfaces. Two axon/ECM contact conditions were investigated: perfect bonding and no bonding. Additionally, axon volume fraction and undulation wavelength and amplitude were varied in this study. The RUC was subjected to normal compressive, normal tensile, and shear loading.

Results: In the baseline case, wavy shock fronts were found in normal compressive and tensile loading, with the axonal shock front preceding the ECM shock front, while a planar shock front was found in shear loading. This waviness increases with wave propagation. Due to perfect bonding, deformation and kinematic quantities were found to be continuous across the axon/ECM interface, yielding a convex axonal shock front and a concave ECM shock front. Large axial stresses were found in the interfacial region, while large compressive stresses were found in both the shock wake and the axon/ECM interface. The von Mises

stress was found to be similar to the 23 shear (σ^{23}), showing that the 23 shear is significant and controls it. The tensile loading case produced 10% lower magnitudes of peak axial tensile stress and 23 shear stress. In the shear loading case, the 23 shear component was found to be larger in axons than ECM, and significantly larger than in the case of axial normal loading. The leading shock front was seen to be followed by trailing release wave. With the introduction of undulated axons, the results did not significantly differ in the cases of normal tensile and compressive loading, but was shown to induce a 75% increase in the magnitude of 23 shear stress in the shear loading case. Manipulating axonal volume fraction did not have a notable effect on the results. Applying no bonding between the axon and ECM revealed a large increase in the von Mises and 23 shear stress as well as multiple instances of peak axial compressive stress in compressive loading, no significant difference in tensile loading, and a 40% decrease in 23 shear stress in shear loading.
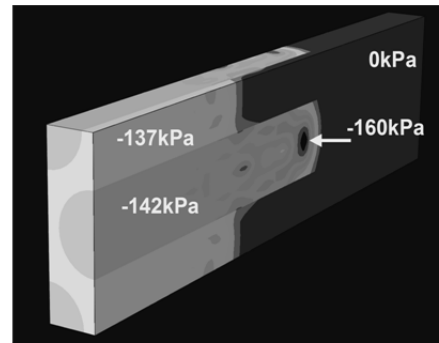

Figure 1. Spatial distribution of the axial normal compressive stress in the baseline case

Conclusions: The results obtained indicate that the presence of undulations within the axons may result in local excursions in the axonal shear stress, the absence of strong axon/ECM bonding can increase the number of locations within the axons at which axial stresses are relatively high, and shear stresses are generally 1-2 orders of magnitude lower than the axial normal stresses within the axons. This finding has to be interpreted while recognizing that axons are generally expected to be more susceptible to injury when subjected to shear rather than axial normal stresses. Unfortunately, axial normal and shear stress injury thresholds with respect to DAI are lacking and therefore it is not possible to discuss if the stress levels observed are of a dangerous level or not.

References: 1. Goel R. MS Thesis, MIT 2011. 2. Holm L. J Rehab Med. 2005;37:131-141. 3. Taber KH. J Neuropsych and Clin Neurosci. 2006;18:141-145. 4. Cernak I. J Trauma Inj, Inf, and Crit Care. 2001;50:695-706. 5. Grujicic M. J Mater and Des. 2010;31:4050-4065.

Efficient Targeting to Bone Tissue for Therapeutic Applications

Erika Jelen, Jhilmil Dhulekar, Margeaux M. Rogers, Thomas L. Moore, Frank Alexis, Bioengineering Department, Clemson University, Clemson, SC 29631

Because an increased of mortality after primary fractures in patients older than 60 years; osteoporotic fracture is a heavy burden on the U.S. economy. This increased in mortality is even higher for patients with repeat vertebral and nonvertebral fractures that occur within 5 years after the first fracture. Although major advances in the understanding of bone biology and osteoporosis have resulted in better diagnosis and treatment, there is clinical evidence that there is a need of safe and effective therapy to reduce the risk of primary and repeat fractures. An innovative area in drug delivery is the use of functionalized nanoparticles to target specific cells or tissues. The first step to develop targeted nanoparticles to bone is to identify and test selecting ligands that have binding affinity in-vitro, ex-vivo, and in-vivo. This research focused on biomolecules with preferential binding to hydroxyapatite (HA), which is the mineral component of bone. The specificity and affinity of the therapeutic delivery could increase the amount of drug delivered to the bone to improve current methods to treat bone diseases. Fluorescent biomolecules were competitively tested using dense HA disks, chicken bone tissue, and mice via local and intravenous (IV) injections. To quantify the binding affinities of the fluorescent peptides, we used the IVIS Lumina XR imaging system equipped with X-ray and fluorescent detection. The results indicated successful peptide binding in all three experiments—HA disks, bone tissue, and mice. Quantitatively, the results show significant differences of biomolecules affinity to bone. The applications for this research include osteoporosis, arthritis, and microgravity-induced bone density loss.

Evaluation of SOD activity in liposome nanoparticles loaded by EUK-134

Raisa Kiseleva, Aleksey Shaporev, Alexey Vertegel
Department of Bioengineering, Clemson University, Clemson, South Carolina 29634

Introduction. Generation of reactive oxygen species (ROS) is increasingly recognized as an important cellular process involved in numerous physiological and pathophysiological processes[1]. Superoxide radicals are one of the most toxic ROS and its damaging effects lead to a variety of detrimental health conditions including cardiovascular diseases, neurodegenerative disorders[2], and extensive oxidative inflammations. The last one can lead to exacerbation of allergic rhinits[3]. Superoxide dismutases (SODs) are a class of metallo-enzymes that catalyze the dismutation of superoxide into oxygen and hydrogen peroxide. Therefore, they play a crucial role in protecting systems against the damage mediated by this deleterious radical. SODs have demonstrated therapeutic efficacy in animal models of some of these disease states[4]. Indeed, the potential therapeutic application of the bovine SOD enzymes for the treatment of human diseases faces several limitations; chiefly among them being the lack of oral activity, the immunogenicity when the SOD derives from non-human sources, short half-lives (they are quickly eliminated from the blood stream), the inability to gain access to the intracellular space of cells where the superoxide radical is produced, and manufacturing costs.

Considering the above, low molecular weight catalysts that mimic the natural SOD enzyme's ability of eliminating superoxide radicals under physiological conditions are actively developing. These types of molecules (SOD mimics) are expected to have considerable therapeutic potential and could also become important probes to elucidate the physiologic and pathologic significance of the intracellular superoxide radical. In this study we investigated the potential of using liposomes loaded EUK-134. This SOD mimetic could replace SOD in antioxidant therapies.

Methods: Liposomes containing EUK-134 was prepared by using the composition of lipids (Cholesterol, PEG and L,a-Phosphatidylcholine) that was dissolved in chloroform and the solvent was removed by rotor evaporation. Solution of EUK-134 in 20 mM HEPES buffer was added to the resulting film with following sonication.

Particle size of prepared liposomes was determined using a 90 Plus dynamic light scattering (DLS) instrument (Brookhaven instruments Corp., Holtsville, NY). Loading yield was measured from UV-Vis spectroscopy data using Synergy HT microplate reader (Bio-tek, Winooski, VT).

SOD activity of EUK-134 was measured using indirect methods involved the enzymatic generation of the superoxide radicals by the xanthine/xanthine oxidase and the use of Cytochrome C (Cyt C) or WST (SOD assay kit, Sigma) as indicators.

Results: The size of liposomes measured using the DLS method was found to be 140±5 nm for both pure liposomes and loaded with EUK-134. The liposomes were purified by dialysis against 20mM HEPES for 6 hours (sufficiency of this duration was proven by UV-Vis spectroscopy). The effective diameter of liposomes remained the same after this procedure indicating the stability of formed liposomes. The encapsulation efficiency and release profile of drug were determined by using UV-Vis spectroscopy. Loading yield of EUK-134 in liposomes was determined to be 15%. Compared with the direct methods, the indirect assays are more commonly used to determine the SOD activity of SOD mimics due to their convenience. Therefore, SOD activity of prepared liposomes was determined by using two methods. It was found, that SOD activity of EUK-134 loaded liposomes was negligible, while EUK-134 obtained upon destruction of liposomes did show SOD activity. This indicates that either SOD radicals cannot penetrate liposomes well or penetration process is slow thus reducing SOD activity to almost zero. The preserved activity of EUK-134 inside liposomes makes it promising agent for protection of cells from oxidative stress when liposomes are adsorbed by cells. SOD inhibition curves revealed some features that EUK-134 has high efficacy in superoxide inactivation, while after certain incubation period its efficacy drops significantly.

Conclusions: Red-Ox activity of liposomes loaded with EUK-134 was observed. SOD assay Kit was used as the standard method to determine SOD activity of prepared liposomes. In this case we had interference of EUK-134 solution with formazan dye which was used as the colorimetric indicator. This result can be explained by the fact that an SOD mimic is reducing superoxide molecules and generates hydrogen peroxide, which could act as either oxidizer or reducer in this system. Kinetic study of EUK-134 release from liposomes loaded with this SOD mimetic shows perspective potential for using of them in targeted drug delivery. Considering all the above, parallel studies that will assess all these points should be carried out to unambiguously determine the SOD activity of any putative SOD mimic. The direct study of the putative reactivity of the SOD mimic with the hydrogen peroxide will be continued.

References:
1. A. Galkin, U.Brandt, The journal of biological chemistry, Vol. 280, No. 34, 26, pp. 30129 –30135, 2005.
2. O. Iranzo, Bioorganic Chemistry, 04/2011, Volume 39, Issue 2, pp. 73 – 87.
3. Chemical exposure guidelines for deployed military personnel. In: Medicine UACfHPaP, ed. Version 1.3 with January 2004 Addendum ed; 2004.
4. A.-F. Miller and D.L. Sorkin, Comments Mol. Cell. Biophys. **9** (1997), pp. 1–48.

The Effect of Gold Nanorods and Sample Preparation methods on Porcine Heart Valves

Heather M. L'Ecuyer[1], Edie Goldsmith[2], Delphine Dean[1]
[1]Clemson University, [2]University of South Carolina

Statement of Purpose: As a result of the rising number of older adults, various heart pathologies such as myxomatous valves, congestive heart failure, and calcification, has arisen over the years and pose complex problems to the medical community. Many of these diseases affect the valves of the heart, which are particularly susceptible to changes in tissue mechanical properties, such as stiffening, prior to failure. Recently, gold nanoparticles and nanorods (AuNRs) have gained interest and favorability in the research field due to their unique optical properties, customizable and flexible size and surface properties, and easy synthesis. [1] This interest led Wilson et al. to discover that AuNRs coated with polyelectrolyte multilayers comprised of either poly(styrene sulfonate) (PSS), or [poly(diallyldimethylammonium chloride) (PDADMAC), will reduce the *in-vitro* collagen matrix contraction by valvular fibroblast cells and also alter the expression of various markers. [2] Sisco et al. later indicated that these AuNRs will also alter the mechanical properties of the *in-vitro* collagen matrix, whereby the final mechanical properties are dependent on the terminal layer of the nanorods. [3] This study explores the mechanical properties of porcine mitral and tricuspid valve tissues after sample preparation treatments, as well as the effect that coated AuNRs have on the mechanical properties of porcine valve tissue. Direct mechanical testing on the valvular tissue in a fluid environment was performed using atomic force microscopy or AFM and the average elastic modulus for samples was calculated using the Hertz model for a spherical indenter.

Methods: Mitral and tricuspid valve leaflets were dissected from whole and fresh porcine hearts and cleaned of the chordae tendinae. 5 mm circles were cut out from the leaflets using a standard punch, which were then either glued or placed on microscope coverslips in a petri dish. Some samples contained injections of AuNRs at low (5.6×10^6 total rods/ valve) and high concentrations (5.6×10^9 total rods/valve). The AuNRs were prepared via wet chemical synthesis method [4] and were either coated with PSS or PDADMAC using a layer by layer assembly method. To determine the effect of sample prep and storage, some control (no rod) valves were frozen. Prior to AFM mechanical testing, the samples were placed at 37 °C and 5% CO_2 for 2 hours in Hank's balanced salt solution to allow the frozen samples to thaw. For each of the samples with the nanorods, an effort was made to test both close to and away from the site of injection. Analysis was conducted at 24 hours after injection and at 48 hours after injection of the AuNRs. AFM nanoindentation was performed on all of the tissues studied (5um silicon spherical tip, ~0.12 N/m cantilever). For all of the samples, the elastic modulus of the indentation curve was determined by fitting the first 500nm of the force vs. indentation depth curve to the Hertz Model.

Results: The tissues studied thus far have exhibited a slight difference in stiffness between the mitral and tricuspid valves. There were great differences due to sample preparation; frozen/thawed tissue was orders of magnitude stiffer than fresh tissue samples (Figure 1, red curve). Likewise, gluing a sample down for study, compared to simply setting the sample down on a microscope slide, will alter the stiffness reported by the AFM (Figure 1, yellow curve). PDADMAC coated nanorods did not have any significant effect on tissue properties (Figure 1, blue curve); however, the high concentrations of PSS coated nanorods tended to increase tissue stiffness (Figure 2), which is consistent with the results on collagen gels. [2,3]
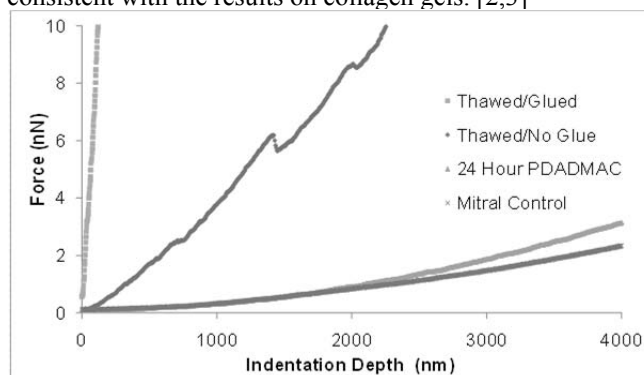

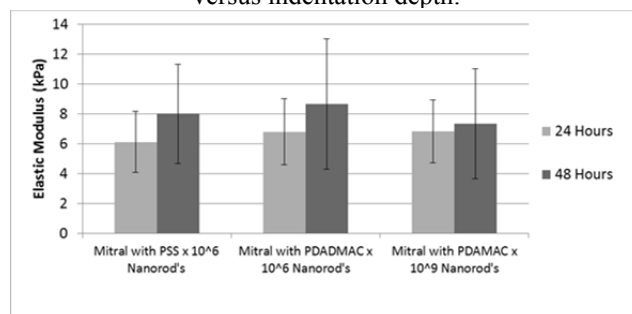Figure 1: Four typical AFM data curves comparing force versus indentation depth.

Figure 2: Bar graph comparing elastic moduli of the samples treated with AuNRs.

Conclusions: Tissue storage and mounting greatly influences measured properties. The results indicate that while PDADMAC nanorods affect collagen gel stiffness, they do not seem to cause any significant changes in valve properties, unlike PSS coated nanorods which significantly increased tissue modulus. Also, it is interesting to note that the side of the valve tested, either the atrial side or the ventricular side, does affect the reported modulus. This is to be expected due to the trilaminar valve structure, and the differences in microstructural fibers present on each side of the leaflet.

References: [1] Chithrani, B. et al. *Nano Letters* 6.4 (2006): 662-68.; [2] Wilson, C.G., et al. *Biomaterials* (2009) 30: 5639-648; [3] Sisco, P. N. et al. *Nano Letters* (2008) 8.10: 3410-412; [4] Jana, Nikhil R., et al. *The Journal of Physical Chemistry B* 105.19 (2001): 4065-067

Development of fiber based biosensors for detecting mRNA molecules in cell lysates

Victor Maximov[1], Yun Xiang[1], Chen-Chih Tsai[2], Konstantin Kornev[2], Alexey Vertegel[1]
[1] Department of Bioengineering, Clemson University, Clemson, SC 29634, United States,
[2] School of Materials Science and Engineering, Clemson University, Clemson, SC 29634, United States
vertege@clemson.edu, vmaximo@clemson.edu

Statement of Purpose: The goal of this study is to develop the novel type of fiber based biosensors for mRNA extraction and PCR analysis from cell lysates obtained from large number of cells.

Introduction: Currently there are many types of biosensors that people use in different areas of research. Biosensors found applications in the agriculture, medicine, protein engineering and food analysis. Usually these biosensors are based on photometric, electrochemical, piezoelectric and others methods of detection of signal. There are many types of biosensors that utilize the enzymes in their sensing part. Recent advances in the biosensors preparation using nano- and microscale materials such as nanoparticles, 1D fibers and 2D matrixes were found to be more efficient. These micro devices require small amount of analyte for analysis and provide great sensitivity and specificity of signal. In current study we were focused on development and testing fiber based biosensors for mRNA extraction from cell lysates. As a model cell culture we have used vascular smooth muscle cells (VSMC), which have two different phenotypes – synthetic and contractile, because the transition between two phenotypes from contractile to synthetic cells is very important and widely investigated model of restenosis. The two phenotypes show different expression levels of many structural proteins such as γ-actin, β-actin, and smooth muscle myosin heavy chain.

Methods: Electrospun fibers made of different polymers (cellulose acetate with addition of polymethylmehacrylate and polyethyleneoxide, polyacrylonitrile) were modified by physical adsorption of streptavidin followed by immobilization of biotin-oligo dT_{25} complex. Fibers were incubated with cell lysates for 30 minutes to allow the reaction of the mRNA's polyA tail with oligo dT to occur. Fibers with attached mRNA were then removed from cell lysates and mRNA extraction was carried out by heating them to 70°C in buffer. Reverse transcription was carried out to transform mRNA to complimentary DNA after mRNA elution. The obtained cDNA was further used in two step PCR reaction to monitor gene expression levels. PCR data was analyzed using the double delta CT method that was developed by Livak and Shmittgen [1]. This method allows one to use variable amount of cells for experiments, detecting the housekeeping gene, which is expressed similarly in both types of cells, as the control. Primary aortic VSMC culture was collected from adult Sprague-Dawley rat and cultured in T75 flasks. Phenotypical change in VSMC culture was induced as it was described previously [2]. Briefly, cells were starved in fetal bovine serum free medium for 15 days to allow them to undergo the phenotypical change. Both starved and fed cell cultures were collected by trypsinisation and lysates were prepared using an ultrasonic homogenizer. These lysates were aliquoted and frozen to use in future experiments.

Results and discussion: We have developed a protocol for mRNA extraction from cell lysates using modified fibers. We have demonstrated that such fiber based biosensors are capable to extract mRNA from VSMC lysates. β-actin mRNA was used as a targeting gene and L32 ribosomal protein mRNA was used as a housekeeping gene and ratio of their expression was monitored.
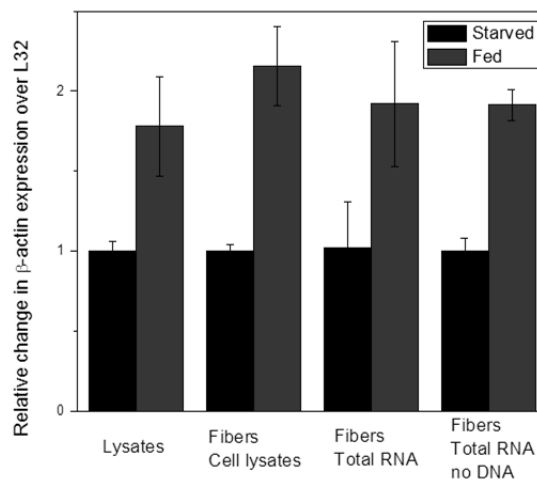

Figure 1. Relative expression of β-actin and L32 mRNA in cell lysates using conventional PCR (left) and different steps of processing of total RNA (n=3)

Figure 1 shows the relative amount of β-actin and L32 mRNA expression in lysates and mRNA extracted by fiber based biosensor from contractile and synthetic VSMC. Ratios of genes expression did not have any significant difference ($p < 0.05$) for the analyzed genes using conventional PCR (left) and fiber-based PCR (second from the left). This experiment was done using a large amount of cell lysates, corresponding to ~10^7 cells.

Conclusions: In conclusion, we have successfully developed fiber based biosensors for mRNA extraction from cell lysates. Cellulose acetate fibers with PMMA and PEO outperformed other types of materials, showing the most consistent data.

References:

[1] K. J. Livak. *Methods* V.25 No.4 (2001), 402-408.
[2] J. D. Hemmer. *Proc. Inst. Mech. Eng. H.* V.222 No.5 (2008), 761-72.

COMPARISON OF MEASUREMENT TECHNIQUES FOR GENERATING QUANTITATIVE TOPOGRAPHICAL MAPS OF EXPLANTED MEDICAL DEVICES

Nunez, Leah, Bryan Thurston, and Dr. Melinda Harman
Department of Bioengineering, Clemson University, SC, USA

Introduction

An integral part of studying the impact of physiological loading on medical devices is understanding the manner of their failure. Visual techniques based on optical microscopy have been to characterize specific damage patterns that are evident on the bearing surfaces of orthopaedic joint prostheses. Such techniques have proven useful for quantifying the size and distribution of damage areas on explanted prostheses. However, measurement techniques for generating topographical maps that quantify the three-dimensional aspects of surface damage (damage area and depth) are less common. The overall objective of this study is to develop a method for generating quantitative topographical maps of explanted prostheses. To do so we will evaluate the accuracy and effectiveness of three image-based methods (CT Scanning, Laser Scanning, and Stereophotogrammetry) and two contact-based methods (Stylus coordinate-measuring, and cast molding) used to acquire three-dimensional representations of surface geometry and damage.

Materials and Methods

This study will involve four phases of assessment. The first phase requires detailed evaluation of equipment performance, resolution, and cost for each of the five methods. The second phase requires generation of suitable measurement phantoms with known dimensions and geometry. The third phase includes application of the different acquisition methods to the phantoms. The final phase requires identification of suitable image registration and contouring software to complete the measurements and to assess the accuracy and repeatability of each method.

Results

Over the course of the next two months, we aspire to complete the initial three phases of this study. The measurement phantoms with known dimensions and geometry will act as the control specimens and will be manufactured with tolerances similar to those existing in bearing materials used in joint replacement. We will image the phantoms utilizing each of the three image-based methods and two contact-based methods. We will compare their accuracy and resolution based on the known dimensions and geometry of the phantoms in order to determine which methodology is the most reliable and efficient way for generating quantitative topographical maps. The contact-based Stylus coordinate-measuring method is currently the most common and accepted method for completing these measurements in our laboratory. Therefore, the results obtained using this technique will form the basis of our comparisons.

Conclusion

We will determine which quantitative topographical mapping method should become the new laboratory standard for imaging the aspects of surface damage (damage area and depth). The selected methodology will be utilized in Total Knee Replacement (TKR) and Reverse Shoulder Implant damage pattern studies to assess polyethylene insert damage.

Using AFM to assess the effect of microbial activity on soil electrical properties

Ruikai Chen[1], Na Hao[2], Matt Cupelli[1], Stephen Moysey[2], Delphine Dean[1]
[1]Departments of Bioengineering and [2]Environmental Engineering Clemson University, Clemson, South Carolina

Statement of Purpose: The purpose of our project is to improve our understanding of microbes and their impact on the subsurface of environment. Spectral induced polarization (SIP) is a geophysical method that can provide non-invasive, but indirect electrical sampling of these processes in the subsurface. To interpret this data at the field scale, there is a need for an improved understanding of how microbial processes alter the electrical properties of rocks. Our approach is to use Atomic Force Microscope (AFM) to analyze how surface topography and electrical properties are affected by microbial mechanisms, providing the quantitative data necessary to connect how the small changes created by microbes could affect the large scale SIP measurements carried out in the field.

Methods: Gold-coated tips were modified with carboxyl terminated self-assembled monolayers. Four NaCl solutions with different concentrations were made so as to compare surface charge of samples as a function of ionic strength (0.001M – 1M NaCl). We have performed SIP experiments using glass beads for four different experimental conditions which mimic changes seen with microbial activity on soil particles: (1) unaltered glass beads, (2) etched beads, (3) calcite precipitation on the beads, and (4) coating the bead surface with iron oxide. 400 point surface charge density maps were obtained as a function of ionic strength (0.001–1M NaCl) by converting a force map using linearized Poisson-Boltzmann theory. In addition, conductive AFM was used to measure surface conductivity maps and, at certain points, current-voltage curves were acquired by applying a surface bias. By collecting these necessary data, we can determine the spatial statistics of complex conductivity on the surface of grains and then compare to SIP measurements on columns of the same glass beads.

Results: Overall, the surface roughness of different glass beads vary a lot and it increases with the bead's size. Interestingly, although the beads had significant roughness and small scale features, the surface charge and conductivity were relatively uniform over the bead surface. The current on the surface are consistent since no microbial activity affects the beads yet. Sample topography, current map of surface are shown in Figure1. Current experiments are underway with glass beads which have been incubated with Sporosarcina pasteuri bacteria.
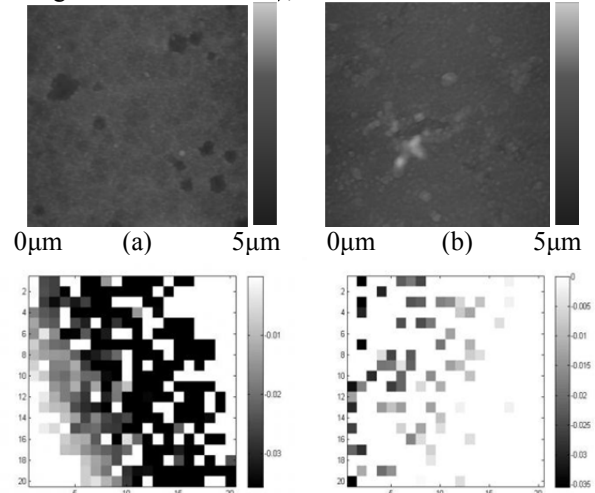

Fig. 1 Height image (5mm scan) of a)0.2mm clean glass beads b)0.2mm etched glass beads. Graphs below are the charging map of them in 1M NaCl.
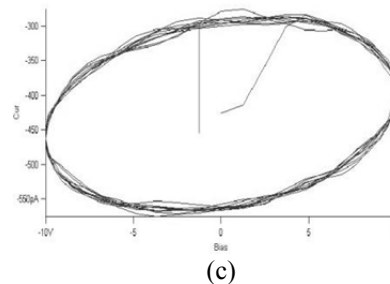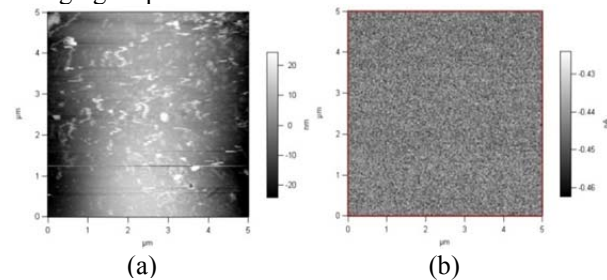

(a)   (b)

(c)

Figure1. a) Height image (5μm scan) of 0.2mm pure glass beads b) Current map of 0.2mm pure glass beads under 10V bias . c) Current curves versus voltage at certain interested points on beads (100Hz sinusoidal bias)

Conclusions: In our first step, we have noticed a correlation between the small scale AFM measurements and the macroscale SIP measurement. After culturing bacteria, we can compare topography and electrical properties between beads with and without bacteria which will give us a direct version of how microbial activities affect biogenic heterogeneities in variation of polarization. This could have potential application for monitoring biogeochemical processes related to transport of groundwater contaminants.

References: 1. Bartosik, E.; Kendall, T.A., 2007, *American Geophysical Union Fall Meeting*.

	Clean 0.2mm	Etched 0.2mm	Clean 1mm	CaCO3 1mm
R_q (nm)	35.1	43.0	234	467

Table. 1 The relative surface roughness of different Glass Beads were compared

Comparison of Achilles Tendon Suture Repair Techniques and Materials:
Krackow vs. Modified Mason-Allen and Fiberwire vs Ethibond Under Cyclic Loading in an *In-Vitro* Bovine Model

Roy J. Rusly[1]; Jong T. Kim[2]; Kara Fruscello[3]; Thierry Bacro[2]; William R. Barfield[1,2,3]; William K. McKibbin[2], John D. DesJardins[1,2]
[1]Department of Bioengineering, Clemson University, Clemson, SC, [2]Medical University of South Carolina, Charleston, SC, [3]College of Charleston, Charleston, SC

Introduction: The annual incidence of Achilles tendon ruptures has been estimated to range between 5.5 and 9.9 ruptures per 100,000 people in North America [1]. Although the appropriate treatment for Achilles tendon rupture remains controversial, many surgeons opt for operative management in active young patients [2]. A good suture technique should provide a high tensile strength, high resistance to gap formation, and minimal suture material on the tendon surface so as not to interfere with tendon gliding and healing [3]. Minimal gap formation between the ends of the repaired tendon is believed to be important during the early post-operative stage in order to effectively facilitate the natural healing process. The Krackow technique is a locking loop suture technique commonly used in tendon repair. Although Krackow is known to produce excellent pullout resistance, it has poor resistance to gap formation [3]. The modified Mason-Allen technique has a less complex suture pattern and is less invasive on the tendon and the connecting tissues, but its use in the repair of acute Achilles tendon ruptures has not been well described in biomechanical literature. This study compares the tensile strength and gap formation resistance of the modified Mason-Allen and Krackow suture technique in an *in vitro* bovine model to benchmark the potential use of the modified Mason-Allen technique clinically. In addition, the effect of two commonly used suture types, Fiberwire and Ethibond, will also be compared to assess their biomechanical performance in these procedures.

METHODS: Ten freshly slaughtered bovine Achilles tendons with attached calcaneus were obtained, and a mid-length tenotomy was performed with a scalpel approximately 3cm above the calcaneus. Two groups of 5 were randomly assigned and repaired with either the Krackow or the modified Mason-Allen techniques using a single Fiberwire suture, providing 2 core strands. The calcaneous was potted in bone cement, and the free tendon end was free-clamped just prior to testing. Each specimen was preloaded with 10N for 5 minutes to reduce creep associated with *in vitro* testing. All specimens were cyclically loaded with a 1 Hz sinusoidal waveform from 10N to 60N for 3000 cycles using a servohydraulic testing machine (Instron-Model #8874). Proximal and distal ends of the tenotomy site were marked at equal distances from the tenotomy site to the center of the tendon and tracked with video extensometry. Specimens were then pulled to failure at 1mm/sec. Failure was defined as a significant change in the slope of the tension-time curve. For the suture comparison study, five additional matched pairs (left and right) of bovine Achilles tendons were repaired with the modified Mason-Allen technique using either Fiberwire or Ethibond, and cyclically loaded and pulled to failure using the same testing techniques as before. Statistical differences between each group were assessed using paired Student-t tests (α=0.05).

Figure 1: Modified Mason Allen Suture Technique

Figure 2: Krackow Suture Technique

Figure 3: Tendon undergoing testing with freeze clamps in a servohydraulic testing machine

RESULTS: Cyclic loading resulted in an average gap of 7.72 ± 0.76mm for the Krackow group and 4.56 ± 0.77mm for the modified Mason-Allen group ($p < 0.010$). The average load at failure for the Krackow group was 238.58±32.61N and for the modified Mason-Allen group was 238.61± 62.86N ($p = 0.999$). Cyclic loading resulted in an average final gap of 4.64±0.48mm for the Fiberwire group and 4.58 ±0.29mm for the Ethibond group ($p = 0.821$). The average load at failure for the Fiberwire group was 242.49 ± 33.19N and for the Ethibond group was 117.50± 6N ($p <$
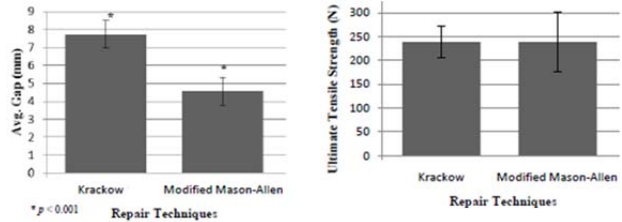

Figure 4- Average gap formation of the Krackow vs. the Modified Mason-Allen Suture Technique

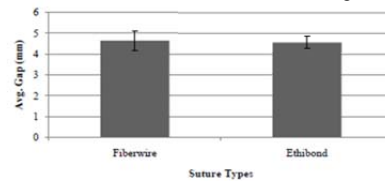Figure 5- Average ultimate tensile strength of the Krackow vs. the Modified Mason-Allen Suture Technique

Figure 6- Average gap formation of the Fiberwire vs. the Ethibond sutures using the Modified Mason-Allen Technique.

CONCLUSIONS: The results show that the modified Mason-Allen suture technique maintains a significantly smaller attenuation at the repaired ends under cyclic loading compared with the Krackow suture technique. The attenuation may be explained by both suture pull-out from the tendon repair construct (due to tightening of the loop and/or tearing of tendon fiber) and the amount of tendon and suture incorporated into each repair [4,5]. In this study, the ultimate tensile load in a repair appears to depend primarily on the suture material and the number of core strands crossing the repair site more so than the suture technique or configuration [6,7]. However, as the number of sutures increases, it is also possible that the suture technique itself becomes the dominating factor since the pullout strength also depends on how well the suture technique holds the soft tissue and minimizes tissue tearing along the fibers at higher load. The suture comparison study shows that Fiberwire suture has a greater inherent tensile strength compared to Ethibond suture while both provide comparable resistance to repair attenuation. In the future, a prospective randomized controlled trial comparing the different repair techniques with identical accelerated rehabilitation protocol could be performed to demonstrate if a particular repair technique might yield superior clinical outcomes.

REFERENCES: [1] Glazebrook, AAOS Now, 2010. [2] Herbort et al, Orthop. Trauma. Surg. 2008;128**:**1273-1277. [3] Barmakian et al, J. Hand Surg. 1994;19A:777-781. [4] Benthien et al, Foot Ankle Int. 2006. 27**:**512-518. [5] Yamagami,et al, . Orthop. Sci. 2006; 11**:**614-619. [6] Mccoy et al, Foot Ankle Int. 2010;31:701-705. [7] McKeon et al, Arthroscopy. 2006;22:33-37.
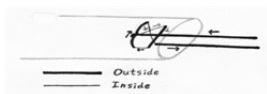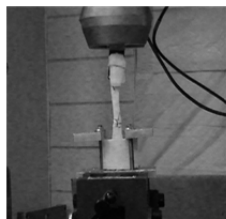
The Application of Nanofibers in Rapid Immunoassays

Ryan Waddell[1], Vladimir Reukov[1], Chen-Chih Tsai[2], Konstantin Kornev[2], Alexey Vertegel[1]
[1]Department of Bioengineering, Clemson University, Clemson, SC 29634, United States,
[2]School of Materials Science and Engineering, Clemson University, Clemson, SC 29634, United States

Statement of Purpose: Diagnostic tests currently use an immunochromatography technique. For instance, pregnancy tests utilize human chorionic gonadotropin (hCG) labeled with gold nanoparticles. These gold conjugates are allowed to migrate along an immunochromatographic strip [1].The purpose of this study is to apply nanofiber yarns in the development of an immunochromatographic test. These yarns would allow the incorporation of diagnostic tests into over-the-counter, household items (e.g. facial tissue) reducing the cost and time required for patient diagnosis. This would lead to earlier treatment ultimately resulting in decreased patient recovery time. These fibers would be beneficial in third world countries with limited availability of funds and medical care. The goal of this pilot study is to demonstrate the viability of incorporating nanofiber yarns in diagnostic tests.

Methods: Rabbit anti-bovine antibody was labeled with gold nanoparticles via physical adsorption. Compatibility of the goat anti-rabbit IgG and rabbit anti-bovine IgG was tested by an immunoprecipitation assay. This was performed by adding a large excess of the goat anti-rabbit IgG to the gold nanoparticle-rabbit anti-bovine conjugates (Au-RaB). The mixture was incubated at 37º C for 30 min with shaking. Immunoassay fibers were produced by immobilizing antibody on poly(acrylonitrile)-cellulose acetate yarns (PAN-CA). Goat anti-rabbit IgG was labeled by Alexa Fluor 594. The labeled antibody was covalently cross-linked to the fiber surface by UV-sensitive Sulfo-NHS-LC-Diazirine cross-linker. A mask placed over the yarn allowed localization of antibody immobilization by blocking UV exposure to the non-specific regions of the yarn. The yarn was then washed with 3% ethanolamine blocking solution to prevent non-specific binding of Au-RaB conjugates. The immunochromatographic assay was conducted by immersing the PAN-CA yarn with immobilized goat anti-rabbit IgG in a solution of Au-RaB conjugates. The yarn was then washed to remove any un-reacted Au-RaB from the yarn.

Results: Fluorescence microscopy confirmed the localized immobilization of the goat anti-rabbit IgG. Results are shown below in *figure 1*.
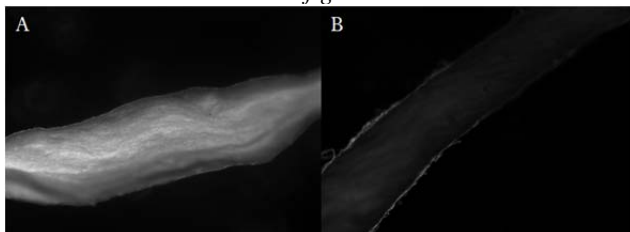

FIGURE 1. Fluorescence of the PAN-CA fiber after antibody immobilization. A) The region of Alexa Fluor 594 labeled goat anti-rabbit immobilization. B) The control region without goat anti-rabbit IgG immobilized.

Reactivity of the Au-RaB with the goat anti-rabbit IgG was confirmed by the immunoprecipitation assay. The immunochromatographic assay showed specific accumulation of Au-RaB at the site of goat anti-rabbit IgG immobilization, as shown below in *figure 2*.
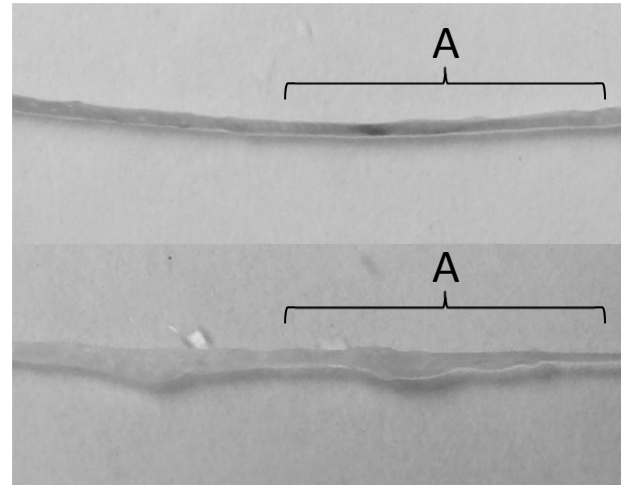

FIGURE 2. PAN-CA fibers after immersion in gold nanoparticle-rabbit antibovine conjugate solution (top) and after washing to remove un-reacted gold nanoparticle-rabbit anti-bovine conjugates (bottom). The goat anti-rabbit immobilized region is represented by [A].

Conclusions:
The fluorescence images of the localized immobilization (*figure 1*) show that PAN-CA nanofiber yarns are a viable material for antibody immobilization, and the method for antibody immobilization allows for localized antibody immobilization on the yarns. The result of the immunoassay (*figure 2*) shows that Au-RaB conjugates can bind to the goat anti-rabbit IgG immobilized on the PAN-CA yarn. Further, the immunoassay shows that the ethanolamine blocking method is a viable method for blocking non-specific binding of the Au-RaB conjugates to regions of the fiber where no antibody is immobilized. Future work will be done to develop isolated control and test lines along the fiber for immunoassay validation. The binding efficiency of the goat anti-rabbit IgG to the PAN-CA fiber needs to be quantified, as well as the optimal quantity of Au-RaB conjugates loaded on the fiber. Future work will also focus on developing a biosensor for detection of specific conditions.

Acknowledgement:

References:
[1] Rojanathanes, R, et al. Taiwan J Obstet Gynecol 2008:147(3): 296-299.

Nitinol Corrosion Ions Inhibit α-actin Expression and Decrease Aspect Ratio of Rat Vascular Smooth Muscle Cells in vitro

Brad Winn, Derrick Quarles, Martine LaBerge, R. Kenneth Marcus.
Department of Bioengineering and Department of Chemistry, Clemson University.

Statement of Purpose: Ni-Ti alloy (Nitinol) has become an increasingly popular biomaterial for use in vascular stenting due to its shape memory properties. However, its high nickel (Ni.) content has been the cause for concern due to possible cell toxicity and alterations in cellular activity. In an effort to understand these interactions between the body and nickel-rich alloys, there have been many in vitro studies evaluating the biocompatibility of Nitinol. Most of these studies evaluated biocompatibility of Nitinol based upon observations such as cellular proliferation, apoptosis, and DNA synthesis. More subtle changes such as altered protein expression are often ignored. This study aimed at developing a clinically relevant in vitro model useful to evaluate the response of smooth muscle cells (SMCs) to varying low levels of Ni ions that should be more representative of tissue concentrations following the implantation of a vascular stent.

Methods: Wire specimens: Nitinol wires (ASTM F2063, Small Parts) 4.4 cm long and 0.127 mm in diameter were ultrasonically cleaned and EtO sterilized. Two wires were then placed in 15 ml conical tubes with 10 ml DMEM (Mediatech, Inc., Herndon, VA, USA) and allowed to corrode for various time periods. At the predetermined time point, the media was removed and transferred to another sterile 15ml conical tube.

Metal Ion Quantification: Metal ions present in the conditioned media were quantified using inductively coupled plasma optical emission spectrometry (ICP-OES) (Ultima 2, Horiba JY, Longjimeau, France). Measurements were taken using a modified protocol developed previously [1].

Smooth Muscle Cell Culture: Aortic smooth muscle cells isolated from female Sprague-Dawley Rats 6-10 weeks of age and maintained with DMEM (10% FBS, 1% Antibiotic-Antimycotic). Cells between passages 4-8 were seeded at a density of 2×10^4 cells/well in a 24 well plate incubated for 48 hours to allow the cells to attach. Following the 48 hr attachment period, the culture media was removed from each well and replaced with 1ml of either control DMEM or corrosion conditioned media samples. The cells were subjected to the test media solutions for a duration of 48 hrs.After the duration of conditioned media exposure, media was removed, and cells were fixed in a 2% paraformaldehyde solution. The cytoskeletal F-actin and cell nuclei were stained using Rhodamine-Phalloidin (Invitrogen, R415) and by 4',6-diamidino-2-phenylindole (DAPI) (Molecular Probes, D-1306, Eugene, OR) respectively. The cells were then imaged using fluorescent microscopy (Nikon Inc., Diaphot 30). ImagePro Plus image analysis software (Media Cybernetics, Inc., Version 5.1, Silver Spring, MD) was then used to measure the major and minor axes of the cells. The aspect ratio was then calculated as the ratio of the major to minor axis lengths.

Expression of α-actin: Cells were immunostained using a primary mouse anti-α-actin antibody with Alexa Fluor 488 tagged donkey anti-mouse secondary antibody. The cells were then DAPI stained to assist in distinguishing individual cells after imaging (Nikon Inc., Diaphot 300, Melville, NY). ImagePro Plus image analysis software (Media Cybernetics, Inc., Version 5.1, Silver Spring,MD) was used to measure the green densitometry of the stained cells. Data were evaluated via ANOVA statistical analysis paired with Tukey analysis using SigmaStat statistical analysis software (Systat Software, Inc., San Jose, CA) with $p<0.05$ indicating a significant difference.

Results:

Ni. ion Concentrations: Corrosion time points of 2, 10, 18, and 31 days were utilized in this study corresponding to Ni. ion concentrations of approximately 0.05, 0.06, 0.08, and 0.15 ppm respectively.

Cell morphology: There was a significant difference in aspect ratio in each group as compared to the standard DMEM control ($P=<0.001$). There does appear to be somewhat of trend of decreasing aspect ratio in response to increasing nickel ion concentration. However, a significant difference was not observed amongst the different experimental groups in response to increasing ionic concentrations. At the highest Ni concentration tested, the mean aspect ratio was decreased by approximately 25% compared to the control.

Expression of α-actin: Interestingly, the most significant difference observed in cell response was with respect to the expression of α-actin ($P=<0.001$). A significant difference in fluorescence compared to the control was observed at all but the lowest concentration of Ni ions tested in this study. Flourescence intensity decreased with increasing Ni ion concentration following a somewhat linear trend ($R^2= 0.86$). At the highest concentration tested, a 26% decrease in fluorescence intensity was observed as compared to the control.

Conclusions: The present study utilized ionic concentrations well below the threshold shown to affect SMC proliferation [2] in an effort to evaluate more subtle effects that such low concentrations have on cell response more likely to carry over into clinical observations. Our results have shown an altered cell morphology as well as decreased smooth muscle cell α-actin expression in response to low nickel concentrations in vitro. It is reasonable to predict that the trends of altered cell morphology and α-actin expression would continue with increasing Ni. ion concentrations. These observations shed some light on one possible contributing factor to the development of in-stent restenosis.

References:

[1] Castro, J. Analytical Methods. 2009. (Vol 1, p. 188-194).
[2] Shih, C. J Biomed Mat Res. 2000. (Vol 52. p. 395-403)

Structural Modeling of Vascular Smooth Muscle Cell Mechanics Using Marc

Scott T. Wood[1], Brian Dean, PhD[1], Shekhar Kanetkar[2], Delphine Dean, PhD[1].
[1]Clemson University [2]MSC.Software

Statement of Purpose: In this study, the nonlinear mechanical behavior of biological cells under dynamic loading are simulated using the finite element analysis (FEA) capabilities of MSC Marc. Vascular smooth muscle cells (VSMCs) are chosen for this study due to the strong correlation of the geometric arrangement of their structural components on their mechanical behavior and the implications of that behavior on diseases such as atherosclerosis [1]. This study is believed to be a significant step towards the viability of finite element models in the field of cellular mechanics because the geometries of the cells in the model are based on confocal microscopy images of actual cells and thus, the results of the model can be compared against experimental data for those same cells.

Methods: Passage 5 – 8 Sprague-Dawley rat aortic VSMCs are cultured in subconfluent layer (~80%) on glass coverslips coated with type I collagen. A contractile phenotype is induced in by incubating the cells for 3 days in a solution of 99% DMEM, 1% anti/anti. Mechanical characterization is achieved using atomic force microscopy (AFM) nanoindentation techniques. Following mechanical characterization, the cells are fixed and stained with AlexaFluor 488 (Invitrogen, Carlsbad, CA) phalloidin to label f-actin and DAPI to label nuclei and imaged using spinning disk confocal microscopy. Geometric characterization of a single VSMC of one physiologically relevant phenotype in 2D cell culture is achieved using confocal microscopy in conjunction with novel image processing techniques. These techniques allow for the creation of representative 3D *in silico* model structures consisting of the cell nucleus, cytoplasm, and actin stress fiber network of each cell, which are then imported into Patran (MSC.Software, Costa Mesa, CA) for structural analysis with MSC Marc. VSMCs are modeled here using a linear elastic material model together with truss elements in Marc which simulate the cytoskeletal fiber network that provides the cells with much of their internal structural support. Material properties for each VSMC model are input based upon values individually obtained through experimentation.
Three model simulations were performed: 1) continuum material properties, 2) compound material properties without an actin network, and 3) compound material properties with an actin network.

Results: A single plane of the actin stress fiber network and nucleus of the cell chosen for simulation are shown in Figure 1, together with the finite element mesh and geometry used for analysis of the cell. The stress and strain from Model Simulation (3) are shown in Figure 2, and the force-indentation curves of all three model simulations are shown in Figure 3.
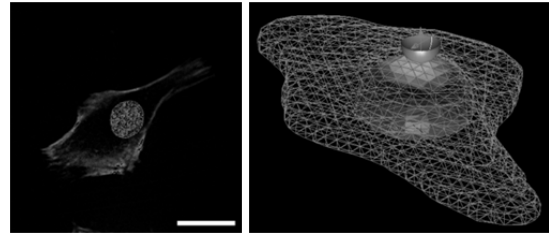

Figure 1. A) Single image plane of the VSMC chosen for analysis B) Geometry and mesh of the cell
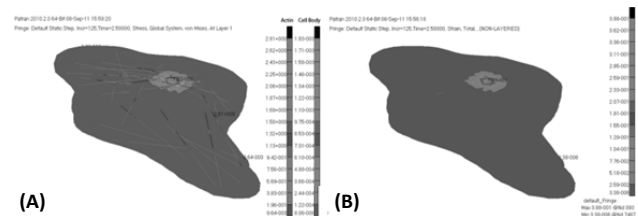

(A)   (B)

Figure 2. Resultant A) von Mises stress and B) strain from Model Simulation (3)
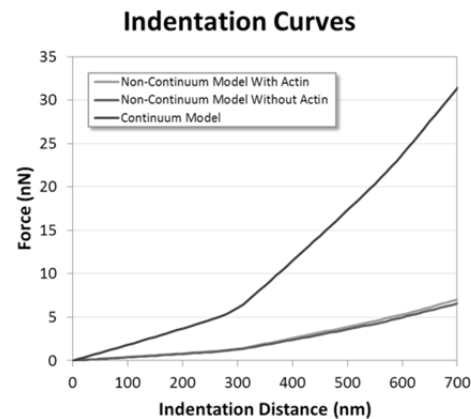

Figure 3. Force-indentation curves of all three model simulations

Conclusions: The model presented in this study is an important step forward toward the ability to use finite element analysis for accurately modeling biological cells and provides a solid foundation from which to build an even more representative model. It is capable of both construction of entirely representative geometries produced in a completely automated manner and validation of its results against experimental data taken from the same cell that was modeled on the same day that the images of the cell were obtained. In future studies, we plan to investigate the influence of actin fiber quantity and thickness on the model, as well as incorporate viscoelastic material properties based on AFM stress relaxation data.

References: 1. Buerke M. BBA. 2007;1774:5-15.

Polymeric nanoparticles and liposoemes for targeted delivery of superoxide dismutase.

Yun Xiang, Victor Maximov, Vladimir Reukov, Alexey Vertegel
Department of Bioengineering, Clemson University, Clemson, SC

Statements of purposes: Enzyme superoxide dismutase (SOD) is well-known for its anti-inflammatory activity. However, the extensive application of SOD is hindered by its poor stability in vivo and often by inability to reach specific site of action. Use of nanoparticles (NPs) and liposomes as carriers can improve stability of protein drugs and, in the case of targeted nanoparticulate carriers, improve their delivery to the desired site. Both targeted and untargeted SOD conjugates have recently been investigated as potential therapeutic agents [1, 2], however, no systematic study of enzyme performance upon attachment to nanoparticles and liposomes has been carried out. The goal of this work is to study effect of different immobilization approaches on enzyme loading and antioxidant activity of SOD-nanoparticle and SOD-liposome conjugates. In addition, the poor stability of the polymer and lipid particles in aqueous suspension is the main problem for the application of such nanocarriers. Moreover, proteins, including enzymes and antibodies conformation, are also more vulnerable in aqueous solution/suspension/environment in long term. Thus, lyophilization of the final product has been commonly applied to achieve longer shelf-life.

Methods: SOD from bovine erythrocytes was purchased from Sigma-Aldrich. We use biodegradable and biocompatible polymers (e.g. PLA, PBCA), and lipids to prepare nanodevices. In our study we prepared two types of nanocarriers – one with SOD encapsulated inside nanoparticles or liposomes, and another with SOD immobilized on the surface. Either UV-sensitive crosslinker or maleimide modified components were applied to immobilize SOD on the nanodevice.

In order to achieve the targeted delivery of SOD, which can decrease the immunogenicity and systemic toxicity of the drug and increase the therapeutically efficacy we modified nanoparticles with antibodies which can specifically bind to targeted tissue. In this study we used NR1 antibody as model, which can be co-immobilized on the surface of nanocarriers along with SOD

During lyophilization, various cryoprotectants, including sucrose and trehalose have been employed in order to achieve proper stability for biopharmaceuticals and to verify the performance of these nano-carriers after the freeze-drying procedure.

Circular dichroism (CD) spectrum measurement in the 190-300 nm region was used to determine the deformation of secondary SOD molecular structure during covalent bonding with nano-carriers.
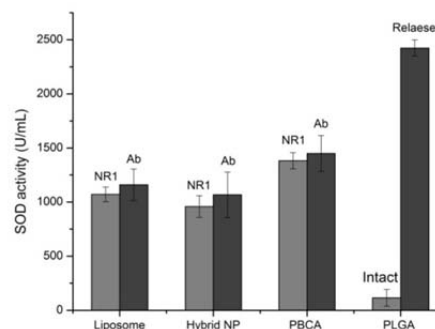

Figure 1. SOD activity of NPs with surface-loaded NPs with antibodies and SOD activity of bulk-loaded PLGA NPs before and after degredation.

Results: As can be seen from the Fig.1. the SOD bulk-loaded PLGA nanoparicles achieved much higher total SOD yield (~3000 U/mL), while SOD activity measured on surface-exposed NPs was around 1000 U/mL. However this graph is also demonstrating that for bulk-loaded NPs, very little SOD activity were detected for the nanoparticles right after the synthesis, and only when the polymer shell was degraded with chloroform and entrapped SOD has been released the high SOD activity has been detected. The additional conjugation with targeted or control antibody does not interfere with SOD activity. The binding yield of around 30% of antibody was achieved. Both sucrose and trehalose showed great cryoprotection effect due to high activity retention (~80%) detected for all samples after lyophilization.

CD spectrum measurement indicated that immobilization on liposomes slightly decreased α-helix and increased β-sheet content.

Conclusion: Nanocarriers with high SOD activity were prepared with conjugated antibodies. The targeting effect to the cells and the free radical scavenging efficiency is to be studied

1.	Reukov, V., V. Maximov, and A. Vertegel, Proteins Conjugated to Poly(Butyl Cyanoacrylate) Nanoparticles as Potential Neuroprotective Agents. Biotechnology and Bioengineering, 2011. 108(2): p. 243-252.
2.	Reddy, M.K. and V. Labhasetwar, Nanoparticle-mediated delivery of superoxide dismutase to the brain: an effective strategy to reduce ischemia-reperfusion injury. Faseb Journal, 2009. 23(5): p. 1384-1395.

Novel T904/fibrinogen hybrid hydrogels for nonviral vector delivery

Jeremy Zhang

Clemson University Department of Bioengineering

Clemson Biomaterials Day Abstract

The long-term goal of this project is to develop biomaterial-based gene delivery systems to increase the expression of survival- and growth-promoting molecules at spinal cord lesion sites and test their ability to increase axonal regeneration. Hydrogels have been widely investigated for localized, sustained delivery of nonviral vectors due to the similarity of their physical properties to native extracellular matrix and their ability to be formed under mild conditions amenable to the incorporation of bioactive molecules. The objective of this study was to develop novel biosynthetic hydrogels composed of both naturally-derived and synthetic polymers for the controlled release of nonviral vectors. Biosynthetic hydrogels were prepared from a synthetic, amphiphilic block copolymer (Tetronic(R) T904) and a natural soluble protein, fibrinogen (FgN). Acrylated T904 was synthesized and crosslinked with fibrinogen in the presence of dithiothreitol and thrombin by simultaneous enzymatic and Michael addition reactions. Plasmid DNA (pGFP) encoding green fluorescence protein and JetPEI/pGFP polyplexes were efficiently loaded and released in the presence of 100 nM plasmin at varying rates as a function of the T904 concentration. At similar gel compositions, the release of pGFP was substantially faster than JetPEI/pGFP polyplexes. T904/FgN hydrogel degradation products were nontoxic and cells grown in close proximity to the hydrogels remained viable and proliferated. B35 and Neuro2A neuroblastoma cells were encapsulated in small fibrin clusters and covered with polyplex-loaded hydrogels. Both cell types progressively degraded and migrated into the hydrogels from the fibrin clusters and increasing GFP expression was observed over the course of two weeks. In conclusion, these studies demonstrate that bioynthetic hydrogels can be formulated to provide controlled release of gene vectors, preserve the bioactivity of released polyplexes, and transfect invading cells during degradation.